Quaternary Science Reviews 186 (2018) 142–155

Contents lists available at ScienceDirect

Quaternary Science Reviews

journal homepage: www.elsevier.com/locate/quascirev

Enhanced Saharan dust input to the Levant during Heinrich stadials

Adi Torfstein [a, b, *], Steven L. Goldstein [c], Mordechai Stein [a, d]

[a] The Fredy & Nadine Herrmann Institute of Earth Sciences, The Hebrew University of Jerusalem, Jerusalem, 91904, Israel
[b] The Interuniversity Institute for Marine Sciences, Eilat 88103, Israel
[c] Lamont-Doherty Earth Observatory and Department of Earth and Environmental Sciences, Columbia University, 61 Rt. 9W, Palisades, NY 10964, USA
[d] Geological Survey of Israel, 30 Malkhe Israel St, Jerusalem, 95501, Israel

ARTICLE INFO

Article history:
Received 23 April 2017
Received in revised form
10 January 2018
Accepted 30 January 2018

Keywords:
Dead sea
Lake lisan
Dust
Sr-Nd-Pb isotopes
Heinrich events

ABSTRACT

The history of dust transport to the Levant during the last glacial period is reconstructed using the isotope ratios of Pb, Sr, Nd, and Hf in sediments of Lake Lisan, the last glacial Dead Sea. Exposed marginal sections of the Lisan Formation were sampled near Masada, the Perazim Valley and from a core drilled at the deep floor of the modern lake. Bulk samples and size fractions display unique isotopic fingerprints: the finest detritus fraction (<5 μm) displays higher $^{87}Sr/^{86}Sr$ and lower εNd values (0.710–0.713 and −7.0 to −9.8, respectively) relative to the coarser fractions (5–20 μm and <20 μm; 0.708–0.710 and −3.4 to −8.3) and the bulk detritus samples (0.709–0.711 and −6 to −7.5). Similarly, the $^{206}Pb/^{204}Pb$, $^{207}Pb/^{204}Pb$ and $^{208}Pb/^{204}Pb$ ratios (18.26-19.02, 15.634-15.68, and 38.25-38.82, respectively) are systematically higher in the finest detritus fraction relative to corresponding coarser fractions and bulk samples.

The $^{87}Sr/^{86}Sr$ and εNd values of the finest fraction correspond with those of atmospheric dust originating from the Sahara Desert, while those of the coarse fractions are similar to loess deposits exposed in the Sinai and Negev Deserts. Pronounced excursions in the Sr-Nd-Pb isotope ratios toward more Sahara-like values coincide with the Heinrich (H) stadials 6, 5 and 1, reflecting significant increases in Saharan dust fluxes during regionally arid intervals, reflected by sharp lake level drops. Moreover, during H6 the dust came from different Saharan sources than during H1 and H5. While the relatively wet glacial climate in the Levant suppressed the transport of dust to the lake watershed, short-term hyper-arid spells during H-stadial intervals were accompanied by enhanced supply of fine Sahara dust to this region.

1. Introduction

1.1. Overview

The Sahara-Arabian desert belt is the largest and most active dust source in the world, and is the primary dust contributor to the Mediterranean and Middle East (e.g., Jickells et al., 2005; Mahowald et al., 2009; Prospero et al., 2002; and references therein), with nearly half a billion tons exported annually (Schutz et al., 1981). Sahara dust fluxes can be influenced by changes in precipitation at the source areas, especially droughts, which lead to reduced vegetation, allowing for increased wind deflation of soils, and ephemeral stream and lake deposits (Prospero and Nees, 1977). Accordingly, the size and location of the desert belt changed on glacial-interglacial timescales (e.g., Gasse, 2000) which was reflected by changes in the production, transport, and deposition of the fine-grain particles that comprise the desert dust. Climate conditions in the potential sink areas could also affect the airborne particle loads. Thus, characterizing the mineralogical, chemical and isotope properties of dust in various geological archives (e.g., lake sediments, deep sea cores, speleothems, ice cores) along with careful consideration of dust mobilization patterns and deposition mechanisms, and their effect on the interpretation of past dust fluxes, can provide important insights into past wind patterns and its relation to regional and global climate patterns.

Overwhelmingly, studies of past dust patterns have focused on bulk or carbonate-leached samples. Although increased attention has been given in recent years to distinguishing between the compositions of different grain size populations (e.g., Grousset et al., 1992; Gaiero, 2007; Meyer et al., 2011; Aarons et al., 2013, 2016; Blakowski et al., 2016; Gili et al., 2016, 2017), such studies

* Corresponding author. The Fredy & Nadine Herrmann Institute of Earth Sciences, The Hebrew University of Jerusalem, Jerusalem, 91904, Israel.
E-mail address: adi.torf@mail.huji.ac.il (A. Torfstein).

https://doi.org/10.1016/j.quascirev.2018.01.018
0277-3791/

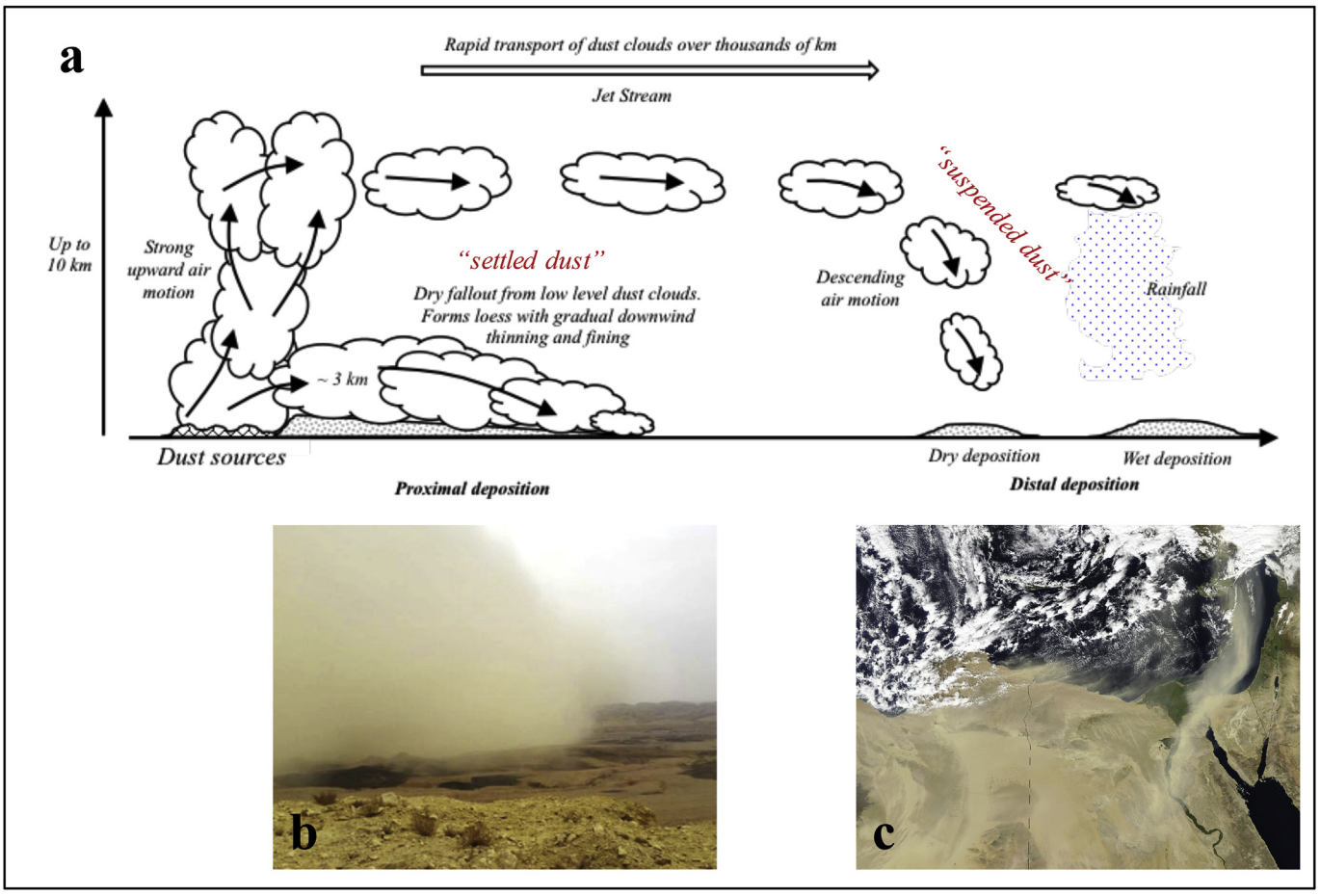

Fig. 1. Schematic model of dust transport mechanisms. Strong low elevation winds are responsible for the transport of silt-sized settling dust originating from the Nile River area, that dominates loess deposits across the Sinai and Negev Deserts, as well as the coarse detritus fraction (>5 μm) of the Dead Sea Basin (DSB) lacustrine deposits. Atmospheric (suspended) dust is raised to high elevations in the source areas and transported toward the DSB where it is exposed to both dry and wet deposition processes. Figure modified after Pye and Zhou (1989). Examples of dust storms associated with (b) settling dust and (c) atmospheric (suspended) dust in the DSB region.

are still limited. This inhibits the ability to distinguish between the geological provenance of two types of dust sources (Fig. 1): (1) far travelled atmospheric dust ("suspended dust") - high-level dust clouds traveling over significant distances of thousands of kilometers, where the deposition of fine particles (<20 μm) is the result of descending air (dry deposition) or rainfall (wet deposition), and (2) dust deposited relatively close to its source ("settled dust") - low level (up to ca. 3 km elevation) dust clouds associated with shorter transport distances, coarser grain sizes, and deposited as dry fallout (Pye and Zhou, 1989). Because each transport mode is controlled by different processes, and their sources are likely different, it is important to distinguish between their histories.

The Dead Sea, a hypersaline terminal lake located in the morphotectonic depression of the Dead Sea basin (DSB), has a large watershed (~40,000 km^2) that extends between the Sahara-Arabian deserts and the sub-tropical Mediterranean climate zone (Fig. 2). During the Quaternary, changing water volumes of the DSB lakes were closely coupled with global and regional climate conditions (e.g., Bartov et al., 2003; Haase-Schramm et al., 2004; Prasad et al., 2004; Stein, 2001; Torfstein et al., 2013b). In particular, the waters of the last glacial Lake Lisan filled the basin and its northward extension (the Jordan Valley), reaching an elevation of up to 160 m below sea level (mbsl), approximately 250 m higher than typical water levels during the Holocene (~400 mbsl). These lake level variations have been interpreted to reflect wetter and drier, glacial and Holocene conditions, respectively, in the lake's watershed.

The Dead Sea lacustrine system is a sink for airborne material from the Sahara-Arabia desert belt, and therefore, the fine-detritus fraction of the lacustrine deposits is a potential archive of past dust fluxes, its changing composition as well as the sources and routes of transport to the Levant over time (Haliva-Cohen et al., 2012). This information allows reconstruction of the atmospheric conditions that prevailed in this region during the late Quaternary. The exposed bedrocks in the Dead Sea watershed are primarily carbonate rocks (limestones and dolomites), with some additional outcrops of Pliocene-Pleistocene basalts in the Galilee and Golan Heights, and sandstones of different ages in the southeast part of the basin. Granitoid outcrops of the late Proterozoic Arabian-Nubian shield (ANS) are exposed along the southeastern margins of the watershed. Previous studies have shown that the fine siliciclastic detritus (termed hereafter "fine detritus") comprises primarily remobilized dust derived from sources outside the basin, mainly from the Sahara and Arabian deserts (Frumkin and Stein, 2004; Haliva-Cohen et al., 2012). In turn, this fine detritus has been used to trace dust sources and transport routes to the Dead Sea watershed and its vicinity (e.g., Frumkin and Stein, 2004; Stein et al., 2007; Palchan et al., 2013, 2018; Ben Israel et al., 2015).

The chemical and isotopic compositions of sediments on earth's surface provide valuable constraints on their provenance, including the source rock composition and age, potential source locations,

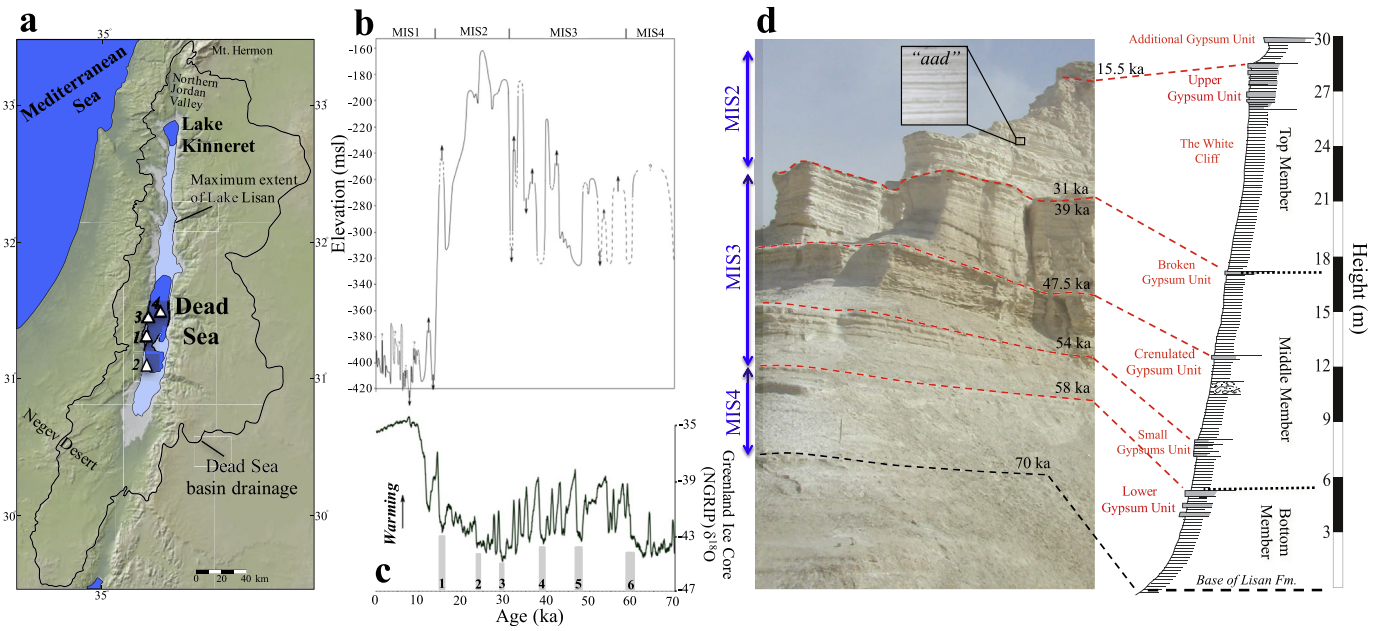

Fig. 2. Location map and Lisan Formation columnar section. (a) Location map. 1- Masada M1 section, 2- Perazim Valley PZ1 section, 3- Ein Gedi, 4- DSDDP coring site. (b) Lake level curve (Modified after: Bartov et al., 2003; Kushnir and Stein, 2010; Migowski et al., 2006; Torfstein et al., 2013b). The dashed curve marks intervals where the lake level is constrained by relatively few observations, and arrows mark the minimal amplitude of an identified fluctuation (see Torfstein et al., 2013b for more details). (c) Greenland Ice Core $\delta^{18}O$ record (Wolff et al., 2010). Grey bars mark the isotopic shifts toward lighter values associated with Heinrich stadials 1–6. (d) Lisan Formation columnar section at the Masada M1 site. Note that the bright-white field appearance of this section stems from the thick sequences of annually deposited alternating aragonite-detritus ("*aad*"; see inset) that are bracketed by the gypsum layers. Gypsum layer names are from Torfstein et al. (2008) and age markers are from Torfstein et al. (2013a). A sedimentary hiatus between 39 and 31 ka is attributed to transgressive erosion processes during the lake level rise towards its MIS2 peak (Torfstein et al., 2013b).

transport history, and exposure to chemical weathering. In particular, the Sr-Nd-Pb-Hf isotopic systems are powerful tracers of the geological history of sediments, and have thus been extensively used to study riverine systems, dust, glacial and marine records (e.g., Goldstein et al., 1984; Goldstein and Jacobsen, 1988; Grousset et al., 1992; Allègre et al., 1996; Hemming, 2004; Grousset and Biscaye, 2005; Gaiero et al., 2007; Gaiero, 2007; Bayon et al., 2009; Hyeong et al., 2011; Aarons et al., 2013; Skonieczny et al., 2013; Kumar et al., 2014; Pichat et al., 2014; Pourmand et al., 2014; Gili et al., 2016, 2017; and numerous others).

Here we report the isotopic compositions of Sr, Nd and Pb, as well as a few Hf isotope ratios, in bulk detritus and three grain-size splits (>20 μm, 20-5 μm and <5 μm) of fine detritus from the last glacial Lisan Formation at the Masada M1 section, spanning the interval between ~70 and 14 ka (Haase-Schramm et al., 2004; Torfstein et al., 2013a). Compositions of bulk detritus samples are reported from additional sites within the DSB (Fig. 2): the PZ1 section at Perazim Valley (Haliva-Cohen et al., 2012) and a core drilled by the International Continental Scientific Drilling Program (ICDP) during 2010–11 in the deep floor of the modern Dead Sea at ~300 m water depth (Neugebauer et al., 2014; Torfstein et al., 2015). The ICDP Dead Sea Deep Drilling Project (DSDDP) retrieved a 456 m thick core spanning the last ~220 ka. The chronologies of the Lisan Formation in each of the above sites has been determined using combined radiocarbon and U-Th dating (Schramm et al., 2000; Haase-Schramm et al., 2004; Torfstein et al., 2013a, 2015), and varve counting (Prasad et al., 2004), and the individual site chronologies were combined to a basin-wide unified chronology with typical age uncertainties between 0.5 and 1 ka (Torfstein et al., 2013a).

Our study broadens the scope of the investigation of dust provenance in the DSB by providing new isotopic and chemical constraints on the potential sources of fine detritus particles over time. We explore the implications of the physical sorting of sediments (e.g., grain sizes), distinguish between the histories and provenance of atmospheric and settled dust found in the DSB, and examine intra-basinal variations in the geochemical properties of the particles (e.g., marginal compared with the center of the lake), in the context of regional hydroclimate conditions.

1.2. Lake Lisan and the Dead Sea

The paleo-hydrology history of the Levant region has been studied in the lacustrine sedimentary sequences that filled the DSB (Stein, 2001; Bartov et al., 2003; Enzel et al., 2003; Bookman (Ken-Tor) et al., 2004; Migowski et al., 2006; Enzel et al., 2008; Waldmann et al., 2010; Kushnir and Stein, 2010; Torfstein et al., 2013b, 2015) and in proximal cave deposits (Bar-Matthews et al., 2003; Vaks et al., 2003, 2006; Lisker et al., 2009). Water levels of Lake Lisan were significantly higher than those of the Holocene Dead Sea (Fig. 2b), reflecting an overall wetter climate in the Dead Sea watershed during the last glacial (Enzel et al., 2008; Stein, 2014; Torfstein et al., 2013b and references therein). Relatively wet conditions prevailed in the watershed during MIS4 (~70–58 ka), followed by abrupt oscillations between wet and dry conditions during MIS3 (~58–30 ka), and wetter conditions during MIS2 (~30–14 ka) (Bartov et al., 2003; Torfstein et al., 2013b). After a peak lake level was reached ~27–25 ka ago (~160 mbsl), the lake level declined to its low Holocene levels (~400 mbsl), while experiencing abrupt vertical oscillations. For example, an abrupt drop occurred during Heinrich (H) stadial 1 and a lake level rise occurred during the Younger Dryas (YD) (Stein et al., 2010).

Due to the large fluctuations, the terminal nature of the lake and the basin morphology, the lake levels are sensitive monitors of hydrological conditions in the Dead Sea basin. Combined with the occurrence of primary (evaporitic) minerals in the sediments (e.g., primary aragonite) that provide the possibility to constrain the duration of such changes by radiometric dating (e.g., radiocarbon,

U-series disequilibrium), the DSB sediments are robust paleo-hydrological archives. Dead Sea sediments mainly comprise alternating aragonite and detrital laminae (*aad* facies; Machlus et al., 2000), gypsum, salt and detritus material. The *aad* facies indicates a wet hydrological regime, while increased aridity that triggered lake level drops is reflected by gypsum and halite. Thick detritus beds are also associated with low lake level stands, though these could also reflect short-term freshwater floods. Thus, the primary precipitated minerals provide information on the origin and evolution of the water systems (e.g., sources of runoff, freshwater-brine interaction; Katz et al., 1977; Stein et al., 1997), while the mineralogical, chemical and isotopic compositions of the fine detritus reflect its provenance (e.g., Haliva-Cohen et al., 2012).

The Lisan Formation at the Masada M1 section is divided into three stratigraphic units (Fig. 2): The Lower and Upper Members are composed mainly of the *aad* facies, while the Middle Member is characterized by many clastic (sand and silt) layers, and laminated gypsum, as well as *aad* sequences. The Lower and Upper Members are capped by the Lower and Upper Gypsum Units (LGU and UGU), respectively (Torfstein et al., 2005, 2008). The *aad* sequences that characterize the Lower and Upper Members were deposited during high lake-level conditions, corresponding to the colder Marine Isotope Stages (MIS) 4 and 2, respectively. The increased abundance of clastic material such as sands, pebbles and thick sequences of silty detritus in the Middle Member reflects frequent low lake-stand conditions that prevailed during the warmer MIS 3 (Bartov et al., 2003; Haase-Schramm et al., 2004).

The elevation of the base of the Lisan Formation at M1 is at 374 mbsl, some 70 m lower (deeper in the paleolake) than the base of PZ1 at 306 mbsl (Torfstein et al., 2013a), and more than 400 m higher than the top of the DSDDP core, whose capping unit was extracted from a water depth of 297 m, at an absolute elevation of 725 mbsl (Torfstein et al., 2015).

1.3. Modern and paleo-dust archives in the levant

Modern dust is transported to the Near East mainly from the Sahara and Arabia deserts (Ganor and Mamane, 1982; Dayan, 1986; Ganor and Foner, 2001; Israelevich et al., 2003). Suspended dust collected during dust storms in Israel is characterized by grain diameters smaller than ~3–4 μm (Kalderon-Asael et al., 2009) and Sr isotope ratios of the silicate fraction in the range of ~0.710–0.720 (Rabi, 2004; Box et al., 2011).

Investigations of paleo-dust transport to the Levant have utilized several potential "dust archives" such as deep sea cores in the east Mediterranean and the Red Sea (Stein et al., 2007; Revel et al., 2010; Box et al., 2011; Palchan et al., 2013), lake sediments (Haliva-Cohen et al., 2012), loess deposits (Haliva-Cohen et al., 2012; Ben Israel et al., 2015) and speleothems (Frumkin and Stein, 2004). The latter study reported results from the Jerusalem (Har-Nof) cave where $^{87}Sr/^{86}Sr$ ranges between ~0.7082–0.7085 during glacials, and below 0.7080 during interglacials, corresponding to the Sr isotope compositions of terra rossa soil above the cave (0.7087) and the Cenomanian dolomitic caprock of the cave (0.7076), respectively. Frumkin and Stein (2004) suggested these results reflect both the hydrology in the source regions, where the glacial desiccation of lakes and marshlands in the Sahara Desert, in combination with strong gusty winds, promoted stronger deflation and transport of dust from the Sahara to the Near East, where this dust settled and formed (via pedogenesis and leaching of carbonate) loess or terra rossa soil. By contrast, during interglacials, lesser amounts of dust were blown to the region and the general aridity did not support pedogenesis and formation of terra rossa soil. Thus, Frumkin and Stein (2004) suggested that the primary source of trace elements in the speleothems was from the leaching of the exposed dolomite caprock.

A study of the petrography, mineralogy, grain size, chemical composition and Nd and Sr isotope ratios of several fine-grained detritus samples from the Ze'elim (Holocene Dead Sea) and Lisan Formations (Haliva-Cohen et al., 2012) found that the detritus consists mostly of silt-size quartz and calcite grains, with a minor presence of clays. The fine detritus in the glacial Lisan Formation shows high $^{87}Sr/^{86}Sr$ and low εNd values that can be linked with Sahara (granitoid) sources while the (fewer) interglacial samples show lower $^{87}Sr/^{86}Sr$ and higher εNd values, similar to compositions of loess deposits from the northern Negev desert. Haliva-Cohen et al. (2012) further proposed that the loess represents a mixture of Nile sediment material (which in turn comprises a mixture of basaltic and granitic sources) that accumulated along the Nile valley, delta and the Mediterranean continental shelves. The Nile deposits were remobilized eastward during glacials, when sea-level was low and the shelves and Nile delta were exposed, and remobilized again during following interglacials by seasonal floods that washed the loess material to the Dead Sea.

2. Methods

2.1. Sample processing

Sample preparation, chemical processing, and chemical and isotopic analyses were performed at the Lamont-Doherty Earth Observatory. For each sample, approximately 500–1000 mg of homogenized powder of bulk sediment was leached with buffered acetic acid until all carbonate was removed. Subsequently, the samples were rinsed twice in MQ water, freeze dried, and weighed again. The insoluble (silicate) fraction of the last glacial Lisan Formation samples comprises ~10–60% of the initial sample weight, compared with 3–13% ($n = 3$) for the Ze'elim Formation, reflecting the variability of the mineral distribution in the sediments (mainly calcite, quartz and clays) (Table 1). The (silicate) residue was homogenized and about 150 mg were wet sieved through a 20 μm sieve. The fine fraction was suspended in DI water with a dilute anti-flocculent (0.05% sodium hexametaphosphate) at 22 °C, and separated into 20-5 μm and <5 μm grain-size fractions by standard Stokes Law settling procedures. Overall, the Lisan Formation samples are dominated by fine silt and clay size particles, whereby the <5 μm, 5–20 μm, and >20 μm weight content is on average 36 ± 14% (1σ), 58 ± 13%, and 6 ± 4%, respectively (Table 1). Previous grain size analyses performed using a Mastersizer on bulk Lisan Formation detritus (Haliva-Cohen et al., 2012) found a dominant grain size mode of ~8 μm. For some samples from the Masada section the *bulk* acid leached residue was digested in addition to the grain size splits. In the rest of the study sites, the acid leached bulk residue was digested.

For digestion, a mixture of HF-HNO_3-$HClO_4$ was added to the samples in Teflon Savillex vials, and left on a hotplate at ~150 °C for several days. Then the sample was dried and a fresh acid mixture added and the vials were returned to the hotplate. Usually, full digestion was achieved within 2–3 such cycles, after which the sample was fully converted into nitric form. Some samples were also exposed to microwave pressure digestion, using the same mixture of acids.

2.2. Chemistry and mass spectrometry

2.2.1. Chemistry

The dried digested samples were diluted in 0.7N HBr and the solution was taken through a series of purification steps to separate the Pb, Sr, Nd and Hf fractions. First, Pb was separated using a 100 μL Teflon columns with AG1 X-8100–200 mesh anion resin; the

Table 1
Sample details. Ages after Torfstein et al., 2013a.

Sample name	Color	Field Description	Location	Height (cm)	Age (ka)	Bulk detritus	>20 um	20-5 um	<5 um
						% ins. residue	% of residue	% of residue	% of residue
Dsen A10u 13.7	v. dark brown	detritus	Ze'elim Fm.	3500	7.4	13.4	3.1	82.3	14.6
Dsen A10 13.12	brown	detritus	Ze'elim Fm.	3500	7.4	2.8			
Dsen A 13u 13.5	light brown	detritus	Ze'elim Fm.	3500	7.4	3.8	9.0	79.3	11.7
MS 200 D-6.3	brown	detritus 6.3 cm from block base. Very soft lamina	Lisan Fm. (M1)	2936	14.4	33.5	2.9	44.6	52.6
MS 282 D-3	light brown	thick detritus 3 cm from block base	Lisan Fm. (M1)	2905	14.8	43.9	1.5	52.0	46.5
MS 280 D-14.5	brown	thick detritus 14.5 cm from block base	Lisan Fm. (M1)	2880	15.1	48.3	1.6	45.8	52.6
MS 205-1	v. light brown	very small block	Lisan Fm. (M1)	2860	15.4	42.2	4.7	56.5	38.8
MS-180 D-0.3	v. light brown	thick detritus 0.3 cm from block base	Lisan Fm. (M1)	2807	15.9	22.1	2.2	60.6	37.2
MS 170 D-11	v. light brown	thick detritus 0.3 cm from block base	Lisan Fm. (M1)	2787	16.1	24.9	6.4	69.7	23.9
MS 160 D-0	light brown	detritus with gypsum vains	Lisan Fm. (M1)	2752	16.3	16.0	13.9	46.7	39.4
MS 150-8	v. light brown	detritus lamina	Lisan Fm. (M1)	2700	16.8	35.6	3.5	49.3	47.3
MS 150-5	v. light brown	detritus lamina	Lisan Fm. (M1)	2700	16.8	12.4	7.1	57.5	35.4
MS 140 D-6.5	light brown	thick detritus lamina 6.5 cm from base block	Lisan Fm. (M1)	2663	16.9	28.2	4.2	56.7	39.1
MS 130 D-4.5	v. light brown	very thin detritus layer at 4.5 cm from base block. A lot of aragonite in sample	Lisan Fm. (M1)	2654	17.1	40.4			
MS 125 9.3	light brown	detritus lamina	Lisan Fm. (M1)	2615	17.6	50.2	3.9	52.7	43.4
Ms-125-9.7			Lisan Fm. (M1)	2615	17.6	36.9	8.9	77.0	14.2
Ms-125-9.7			Lisan Fm. (M1)	2615	17.6	41.3	7.5	63.7	28.8
MS 120 14.5	v. light brown	detritus lamina	Lisan Fm. (M1)	2505	19.2	37.3	6.2	53.8	40.0
MS-120 D-18.1	v. light brown	detritus at 18.1	Lisan Fm. (M1)	2505	19.2	40.7	2.3	57.0	40.7
MS 120 D-2.5	v. light brown	thick detritus lamina	Lisan Fm. (M1)	2505	19.2	52.1	0.8	74.4	24.8
MS 120 17.0	v. light brown	thick detritus?	Lisan Fm. (M1)	2505	19.2	42.6			
MS 120 13.5b	dark brown	continuation of ms-120-13.5a but brown colored	Lisan Fm. (M1)	2505	19.2	46.3			
MS 120-D	v. dark brown	detritus lamina	Lisan Fm. (M1)	2505	19.2	12.5			
MS-110-D 4.1	v. light brown	detritus lamina	Lisan Fm. (M1)	2375	21.1	49.4	6.2	44.7	49.2
MS 110 D.17	v. light brown	thick detritus layer	Lisan Fm. (M1)	2375	21.1	53.9	6.7	42.3	51.0
MS 100.2 D 8.2	v. light brown	thick detritus lamina relatively brown colored	Lisan Fm. (M1)	2050	25.9	57.8	4.7	63.5	31.7
MS 90 8.5	light brown	thick detritus layer	Lisan Fm. (M1)	1813	29.4	46.5			
MS 800 D-0.1	brown	thick detritus lamina (~3 mm) at block base	Lisan Fm. (M1)	1690	39.0	46.9	11.8	63.2	25.1
MS 700 D-10.5	light brown	thick detritus layer at 10.5 cm from block base. Looks like silt	Lisan Fm. (M1)	1475	42.7	27.6	14.3	59.9	25.8
MS 75 D-16.1	brown	thick detritus 16.1 cm from block base	Lisan Fm. (M1)	1185	48.9	32.7			
MS 75-D	brown	detritus lamina	Lisan Fm. (M1)	1185	48.9	46.3	8.4	62.2	29.4
MS 300-D	light brown	detritus lamina	Lisan Fm. (M1)	675	55.3	35.2			
MS 30 D-7.8	v. light brown	thin detritus lamina 7.8 cm from block base	Lisan Fm. (M1)	554	58.2	8.7			
MS-37	brown	detritus lamina	Lisan Fm. (M1)	546	58.3	60.1			
Ms-37			Lisan Fm. (M1)	546	58.3	36.0	9.2	73.1	17.7

Table 1 (*continued*)

Sample name	Color	Field Description	Location	Height (cm)	Age (ka)	Bulk detritus	>20 um	20-5 um	<5 um
						% ins. residue	% of residue	% of residue	% of residue
Ms-37			Lisan Fm. (M1)	546	58.3	41.3	11.2	66.8	22.0
MS 26-D	dark brown	detritus lamina	Lisan Fm. (M1)	490	59.0	39.0			
MS 10 D-13.2	brown	detritus lamina with gypsum veins above it 13.2 cm from block top	Lisan Fm. (M1)	420	60.0	18.8			
MS 8 D-8.5	dark brown	detritus 8.5 cm from block base	Lisan Fm. (M1)	415	60.1	25.7			
MS 5-D-2	ligh brown	detritus lamina	Lisan Fm. (M1)	275	63.3	17.8			
MS-6	light brown	detritus lamina	Lisan Fm. (M1)	269	63.4	20.1	2.7	52.2	45.0
Ms-6			Lisan Fm. (M1)	269	63.4	17.7			
Ms-6			Lisan Fm. (M1)	269	63.4	20.2			
MS 5-01	dark brown	detritus lamina	Lisan Fm. (M1)	266	63.5	41.0	0.0	25.4	74.6

matrix was eluted with 0.7N HBr, while Pb was eluted with 6N HCl. The eluted matrix solution was then taken through 100 μL Teflon columns with Eichrom TRU-spec resin, and the rare earth elements (REE) were separated from other cations, using 1N HCl and 1N HNO_3, respectively. Then, Sr was purified from the residual cation cut on 30 μL Teflon columns with Eichrom Sr-spec resin, by conditioning with 3N HNO_3 and eluting with water. The REE fraction was carefully dried and brought up in 100 μL of 0.22N double distilled HNO_3. This cut was then passed through 800 μL Savillex columns filled with Eichrom LN-spec resin, and Nd was isolated using 0.22N HNO_3. The residual cuts from all steps were mixed together, dried, and brought up in 5 ml 3N HCl. The solution was subsequently passed through a Teflon column filled with 1 ml of LN-spec resin and Hf collected using a mixed 6N HCl-0.2N HF solution. All resins were pre-cleaned prior to use, and acids used during the purification steps were cleaned by double distillation.

2.2.2. Mass spectrometry

Pb isotope ratios were measured on a VG Axiom multi-collector ICPMS. Mass discrimination was monitored and corrected for using a Tl spike. Replicate measurements of NIST SRM 981 between every one or two samples yielded a typical 2σ standard error of 180 ppm, 220 ppm and 250 ppm for $^{206}Pb/^{204}Pb$, $^{207}Pb/^{204}Pb$, and $^{208}Pb/^{204}Pb$, respectively. All results were normalized to SRM 981 values of $^{206}Pb/^{204}Pb = 16.9405$, $^{207}Pb/^{204}Pb = 15.4963$, $^{208}Pb/^{204}Pb = 36.7219$ (Abouchami et al., 1999). Five separate digestions of an international rock standard BCR2 were processed concurrently with the samples. The results, including duplicate analyses of the same digestion during different measuring sessions, yielded an average value of 18.763 ± 3, 15.624 ± 2 and 38.740 ± 5, for $^{206}Pb/^{204}Pb$, $^{207}Pb/^{204}Pb$, and $^{208}Pb/^{204}Pb$, respectively (2σ, n = 5). These values are consistent, within uncertainty, with previously published values for bulk samples (Baker et al., 2004; Elburg et al., 2005), but differ from those of Jweda et al. (2016), whose Pb isotope analyses were performed on acid leached BCR2 powder.

Sr isotope ratios were measured on a VG Sector 54 multi-collector thermal ionization mass spectrometer, using dynamic multi-collection and an exponential fractionation correction. $^{87}Sr/^{86}Sr$ ratios were normalized to $^{86}Sr/^{88}Sr = 0.1194$. Replicate measurements of NIST SRM 987 yielded an average $^{87}Sr/^{86}Sr = 0.710268 \pm 24$ (2σ, n = 66), and all results were corrected to a value of 0.710244. Seven separate digestions of BCR2 were analyzed, including duplicate analyses of the same digestion during different measuring sessions, and yielded an average value of 0.705001 ± 25 (2σ, n = 13), consistent with the Jweda et al. (2016) value of 0.705000 ± 11.

Nd and Hf isotope ratios were measured on a ThermoScientific Neptune Plus multi-collector ICPMS. $^{143}Nd/^{144}Nd$ ratios were normalized to $^{146}Nd/^{144}Nd = 0.7219$. The JNdi standard was measured between every one or two samples, and normalized to a value of 0.512115 (Tanaka et al., 2000). Analyses of the La Jolla standard yielded a value of 0.511865 ± 22 (2σ, n = 6), in agreement with Jweda et al. (2016) (0.511858 ± 10). Seven separate digestions of BCR2 were analyzed, including two replicate analyses of the same solutions during different measuring sessions, and yielded an average value of 0.512636 ± 34 (2σ, n = 7), identical to the value reported by Jweda et al. (2016). The $^{143}Nd/^{144}Nd$ isotope ratio is expressed as $\varepsilon Nd = [(^{143}Nd/^{144}Nd)_{sample}/(^{143}Nd/^{144}Nd)_{CHUR}-1]x10^4$, where $(^{143}Nd/^{144}Nd)_{CHUR} = 0.512638$ (Wasserburg et al., 1981). A Hf Spex standard solution, which has been calibrated with the JMC 475 Hf standard and found to have the same isotope ratio, yielded an average $^{176}Hf/^{177}Hf$ value of 0.282149 ± 4 (2σ, n = 21), which was corrected to 0.282160. Instrumental mass fractionation of $^{176}Hf/^{177}Hf$ was corrected using the exponential fractionation law and assuming $^{179}Hf/^{177}Hf = 0.7325$. A BCR2 digestion yielded a value of 0.282863 ± 2 (2σ internal error), consistent with the Jweda et al. (2016) value of 0.282866 ± 11. Hf isotopic values are expressed using the εHf, whereby $^{176}Hf/^{177}Hf_{CHUR} = 0.282785$ (Bouvier et al., 2008).

3. Results

Sr, Nd, Pb and Hf isotope ratios of the different grain size fractions at the M1 section (Table 2) show significant differences in the isotope ratios over different time intervals and between the grain size fractions. The range of values for each isotopic system are larger in the grain size fractions compared to the bulk detritus. Moreover, the distinct differences between the isotopic compositions in the different size fractions document different sources and transport histories. At the Masada M1 section (Table 2), the fine fraction (<5 μm) yields the highest Sr isotope ratios (0.7102–0.7131), while the intermediate fraction (5–20 μm) yields intermediate values (0.7093–0.7097) and the coarse fraction (>20 μm) yields the lowest values (<0.709). As expected from these relationships, the values of the bulk detritus samples (n = 11) are

Table 2
Sr-Nd-Pb-Hf isotope ratios of detritus size fractions at M1 section. Individual internal errors (2σ) are typically smaller than the external standard reproducibility.

Sample name	Grain size (um)	Height (cm)	Age (ka)	$^{87}Sr/^{86}Sr$	$^{143}Nd/^{144}Nd$	εNd	$^{206}Pb/^{204}Pb$	$^{207}Pb/^{204}Pb$	$^{208}Pb/^{204}Pb$	$^{176}Hf/^{177}Hf$	εHf
MS 200 D-6.3	<5	2936	14.4	0.712429	0.512234	−7.9	18.8379	15.6765	38.7341		
MS 280 D-14.5	<5	2880	15.1	0.712795	0.512188	−8.8	18.9336	15.6822	38.7943		
MS 205-1	<5	2860	15.4	0.712040	0.512262	−7.3	18.9185	15.6774	38.7590		
MS-180 D-0.3	<5	2807	15.9	0.712471	0.512236	−7.9	18.8924	15.6754	38.7707		
MS 170 D-11	<5	2787	16.1	0.711726	0.512236	−7.8	18.9026	15.6761	38.7785		
MS 160 D-0	<5	2752	16.4	0.711806	0.512200	−8.5	18.8576	15.6786	38.7560		
MS 150-8	<5	2700	16.8	0.711223	0.512162	−9.3	18.8444	15.6755	38.7464		
MS 140 D-6.5	<5	2663	16.9	0.712506	0.512167	−9.2	18.9010	15.6772	38.7651		
MS 130 D-4.5	<5	2654	17.1	0.711655	0.512207	−8.4	18.7927	15.6686	38.6589		
MS 125 9.3	<5	2615	17.6	0.711751	0.512277	−7.0	18.8756	15.6781	38.7954	0.282813	1.0
MS 700 D-10.5	<5	1475	42.7	0.711228	0.512211	−8.3	18.9887	15.6787	38.7879		
MS 75-D	<5	1185	48.9	0.713140	0.512277	−7.1	19.0229	15.6788	38.7364		
MS 300-D	<5	675	55.3	0.710248	0.512152	−9.4	18.6938	15.6639	38.6149		
MS-37	<5	546	58.3	0.711628	0.512195	−8.6	18.5630	15.6497	38.4739		
MS 26-D	<5	490	59.0	0.711991	0.512134	−9.8	18.6666	15.6584	38.5832		
MS 10 D-13.2	<5	420	60.0	0.712243	0.512242	−7.7	18.8032	15.6706	38.7153		
MS 8 D-8.5	<5	415	60.1	0.711405	0.512214	−8.3	18.8404	15.6715	38.7270		
MS 5-D-2	<5	275	63.3	0.710618	0.512222	−8.1	18.7446	15.6711	38.6827		
MS-6	<5	269	63.4	0.711462	0.512183	−8.9	18.2639	15.6385	38.2532		
MS 5-01	<5	266	63.5	0.711927	0.512183	−8.9	18.7509	15.6692	38.6992		
MS 110 D.17	<5	2375	21.2	0.711196	0.512253	−7.5	18.8390	15.6766	38.7548	0.282822	1.3
MS-110-D 4.1	<5	2375	21.2	0.711186	0.512210	−8.3	18.8403	15.6729	38.7499		
MS-120 D-18.1	<5	2505	19.2	0.711824	0.512229	−8.0	18.8326	15.6805	38.7633		
MS 100.2 D 8.2	<5	2050	25.9	0.711208	0.512255	−7.5	18.7923	15.6733	38.6968	0.282823	1.4
MS 800 D-0.1	<5	1690	39.0	0.710616	0.512261	−7.4	18.7564	15.6642	38.6607		
MS 125 9.3	20–5	2615	17.6	0.709293	0.512463	−3.4	18.7316	15.6549	38.6830	0.282503	−10.0
MS 110 D.17	20–5	2375	21.2	0.709593	0.512310	−6.4	18.5020	15.6293	38.3965	0.282499	−10.1
MS 100.2 D 8.2	20–5	2050	25.9	0.709668	0.512215	−8.3	18.7832	15.6652	38.8147	0.282588	−7.0
MS 125 9.3	>20	2615	17.6	0.707870	0.512323	−6.2				0.282487	−10.6
MS 100.2 D 8.2	>20	2050	25.9	0.708541	0.512293	−6.7	18.6889	15.6484	38.3689	0.282428	−12.6

Table 3
Sr-Nd-Pb isotope ratios of bulk detritus at M1 section and Ze'elim Fm.

Sample name	Height (cm)	Age (ka)	$^{87}Sr/^{86}Sr$	$^{143}Nd/^{144}Nd$	εNd	$^{206}Pb/^{204}Pb$	$^{207}Pb/^{204}Pb$	$^{208}Pb/^{204}Pb$
MS 200 D-6.3	2936	14.4	0.710399	0.512283	−6.9	18.8378	15.6694	38.7240
MS 125 9.3	2615	17.6	0.710336	0.512266	−7.3	18.8279	15.6625	38.7171
Ms 75-D	1188	48.9	0.709700	0.512259	−7.4	18.9668	15.6685	38.7601
Ms 37	546	58.3	0.709333	0.512270	−7.2	18.7836	15.6593	38.6763
Ms 26 (264)	488	59.0	0.709380	0.512336	−5.9	18.9334	15.6694	38.7717
Ms 8-c	415	60.1	0.710523	0.512250	−7.6	18.7725	15.6693	38.7381
Ms 110 D17 A	2361	21.2	0.709925	0.512270	−7.2	18.8117	15.6685	38.7255
duplicate						18.8127	15.6692	38.7283
Ms 110 D17B	2361	21.2	0.710030					
Ms 110 D17 C	2361	21.2	0.710037	0.512266	−7.3	18.8157	15.6703	38.7533
Ms 100.2 D8.2 A	2050	25.9	0.709900	0.512280	−7.0	18.8236	15.6694	38.7820
Ms 100.2 D8.2 B	2050	25.9	0.709883	0.512257	−7.4			
Ms 120 D18.1	2506	19.2	0.710120	0.512281	−7.0	18.8335	15.6699	38.7466
DSEn A10 13.70	Ze'elim Fm.	7.4	0.710455	0.512185	−8.8	18.8415	15.6607	38.7437

intermediate (0.7093–0.7105; Table 3). εNd values show complementary relationships, although less distinctly, that is, the fine fraction shows the lowest values, intermediate fraction and bulk samples show intermediate values, the coarse fraction shows the highest values. The full range is between −9.8 and −6.1 (with one outlier at −3.4) (Fig. 3).

The total range of $^{206}Pb/^{204}Pb$, $^{207}Pb/^{204}Pb$ and $^{208}Pb/^{204}Pb$ ratios of the three grain sizes at Masada (Table 2) are ~18.26–19.02, 15.68–15.63 and 38.25–38.81, respectively (Fig. 4). A comparison of the grain size splits of the same sample shows that the coarser fractions are consistently lower than the fine fraction splits (Fig. 5). Moreover, the Pb isotope ratios of the bulk silicate fraction are generally closer to the high range of the <5 μm fraction, reflecting the fact that most of the Pb is located in the fine particles, most likely clay minerals.

The Sr isotope ratios of bulk silicate samples from the Perazim Valley PZ1 section (Table 4) are higher than the Masada bulk samples ($^{87}Sr/^{86}Sr$ in the PZ1 samples are mainly in the range of 0.710–0.712; Fig. 3), while εNd is overall in the same range, between −8.3 and −5.2. Three samples of thick detritus laminae (the laminated detritus ld facies described by Haliva-Cohen et al., 2012) from the interval of ~30–40 ka (Middle Member of the Lisan Formation at PZ1) yield lower Sr isotope values (<0.710) (Fig. 3). Samples from the Lisan Formation interval of the DSDDP core show $^{87}Sr/^{86}Sr$ ratios and εNd values of 0.7085–0.7099 and −5.2 to −6.8, respectively (Table 5; Fig. 3). The $^{87}Sr/^{86}Sr$ ratios and εNd values of the DSDDP samples lie on the lower and higher sides, respectively, of the Masada and Perazim Valley (M1 and PZ1) samples. Despite the limited number of Hf isotope data (8 samples), there are clear differences between the different grain size fractions (Table 2), with a large εHf range between +1.35 (fine fraction) and −12.6 (coarse fraction).

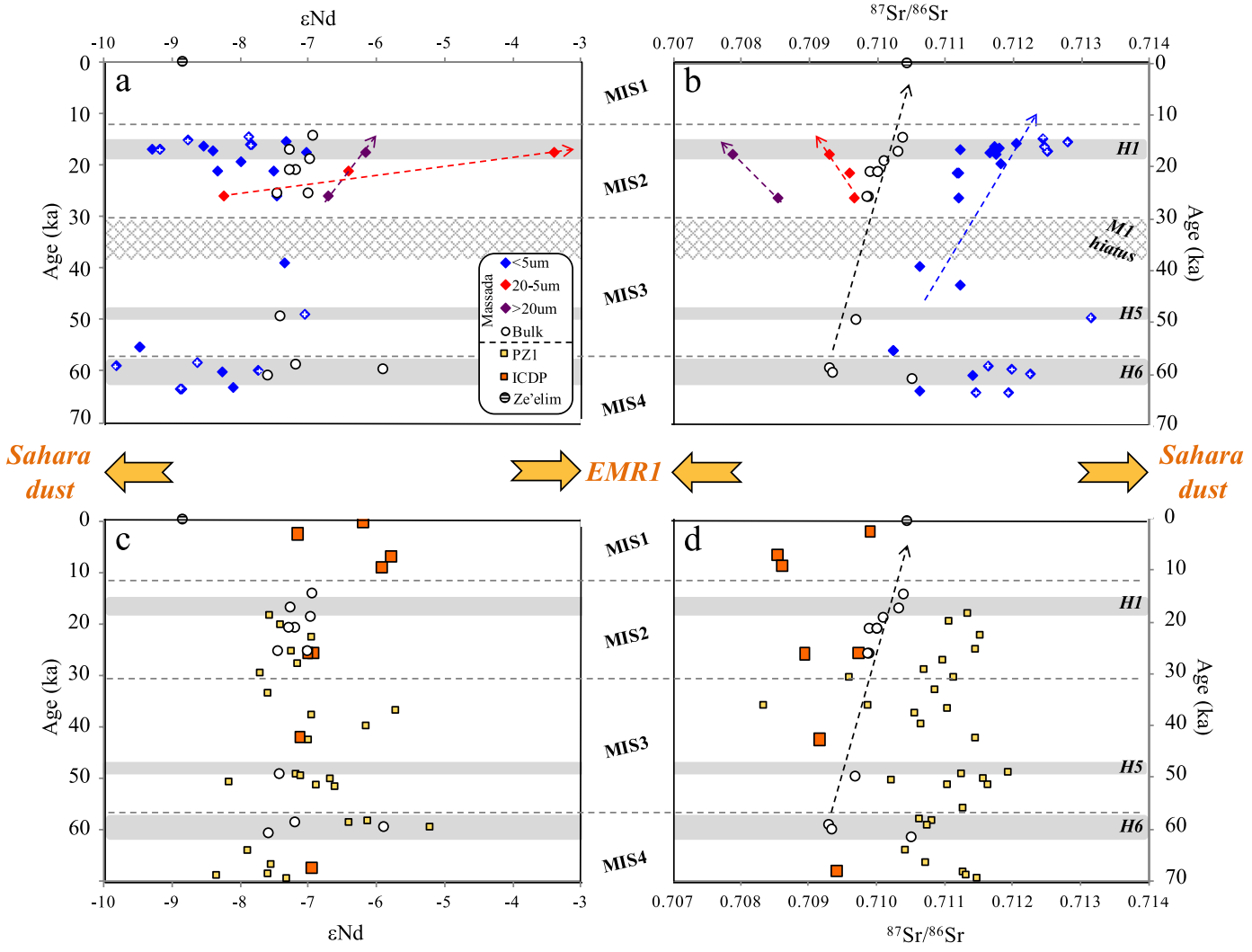

Fig. 3. εNd and $^{87}Sr/^{86}Sr$ over the last 70 ka. (a,b) Bulk detritus and grain size fractions from M1 and Ze'elim, and (c,d) Bulk detritus from M1, PZ1 and the DSDDP core. The horizontal dashed curves mark the timing of the Marine Isotope Stages (MISs) 4,3,2,1 transitions, the grey rectangles mark the timing of Heinrich (H) stadials 6, 5 and 1, and a cross pattern between 38 and 31 ka marks the timing of a sedimentary hiatus in the M1 section. Note that the range of both isotope systems is between two end member compositions marked by yellow arrows: suspended (atmospheric) dust associated with a Sahara Desert end member, and settling dust associated regional loess, and referred to here as End Member 1 (EMR1; see text for details). Blue diamonds with white crosses in (a) and (b) pertain to the samples that are identified to form the "Sahara dust array", as detailed in Fig. 7 and discussed in the text. The red, purple, black and blue dashed arrows mark the secular evolution curves of each isotope system in the 20–5, >20, bulk and <5 μm fractions, respectively. (For interpretation of the references to color in this figure legend, the reader is referred to the Web version of this article.)

4. Discussion

4.1. The Sahara dust array

Considering the combined Sr-Nd isotope ratios (Fig. 6), the Dead Sea lacustrine detritus samples lie along a mixing array defined by a source composition ("end member" on the mixing array) associated with dust particles originating from the Sahara Desert ($^{87}Sr/^{86}Sr > 0.715$ and $\varepsilon Nd < -10$) and one characterized by a $^{87}Sr/^{86}Sr$ range between ~0.708 and 0.707, and εNd between ~−5 and −2. Previous discussions in the literature have associated this latter end member with reworked Nile River sediments and their downwind products, the Negev loess deposits (e.g., Ben Israel et al., 2015; Crouvi et al., 2008; Enzel et al., 2008; Haliva-Cohen et al., 2012). Palchan et al. (2018) suggested that this end member composition is controlled by pedogensis processes affecting settled dust, subsequently forming various types of loess. For the purpose of the forthcoming discussion however, we define this simply as End Member 1 (EMR1), with the understanding that it is broadly associated with the Negev loess deposits. It is also notable that the Sr-Nd isotopic composition of the <5 μm detritus fraction at M1 (blue diamonds in Fig. 6) is more similar to Sahara dusts, while the coarser fractions (5–20 μm and >20 μm, red and purple diamonds, respectively) have lower $^{87}Sr/^{86}Sr$ and higher εNd values, and are closer to the EMR1 composition (Figs. 3 and 6).

The coupled $^{87}Sr/^{86}Sr$ - $^{206}Pb/^{204}Pb$ field yields two mixing arrays (Fig. 7). One shows limited $^{87}Sr/^{86}Sr$ variability (between 0.7115 and 0.7131) compared to a large range in $^{206}Pb/^{204}Pb$ values (18.26–19.02), and is composed of the fine (<5 μm) fraction. This array is highlighted in Fig. 7b by a grey shadow extending between two end members, which we arbitrarily define as EMR2 and EMR3. The samples forming this array are highlighted with a white cross superimposed over a blue diamond, and similar symbols are used to mark these samples in Figs. 4–6. In Sr-Nd isotope space (Fig. 6) these

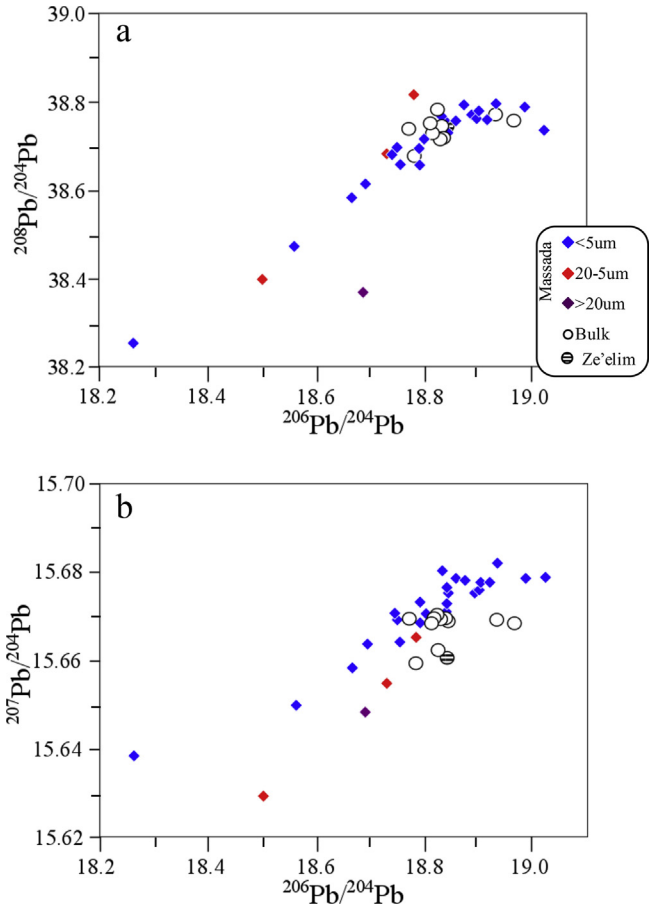

Fig. 4. Pb isotopic compositions of Dead Sea lacustrine deposits. All data points pertain to the carbonate-free (acid-leached) fraction of the sediments.

samples display the strongest influence of a Saharan dust component, and thus we term them the "*Sahara dust array*" (Fig. 7b).

The samples that are not part of the Sahara dust array in Fig. 7 show a range of both $^{87}Sr/^{86}Sr$ and $^{206}Pb/^{204}Pb$ values and the trend, extending between EMR1 and the Sahara dust array, is controlled by the different grain size groups. This mixing array displays considerable scatter relative to the Sahara dust array, probably due to the composition of EMR1 - the regional "loess" component - which appears to be variable and poorly constrained in terms of its Pb isotopic composition.

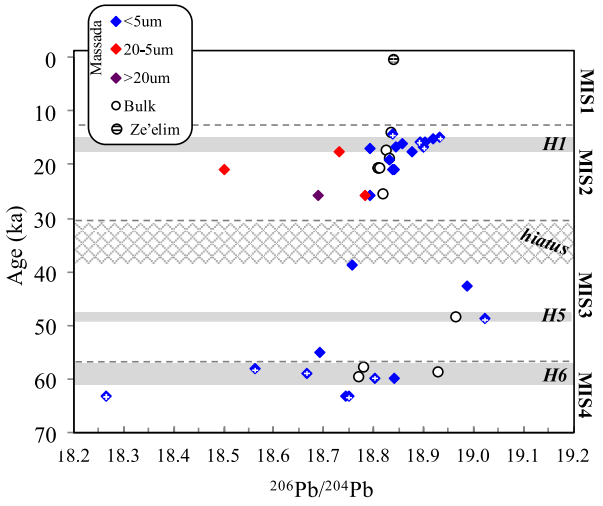

Fig. 5. The secular evolution of $^{206}Pb/^{204}Pb$ over the last 70 ka at M1 and Ze'elim. Blue diamonds with white crosses pertain to samples that are identified to form the "Sahara dust array", as detailed in Fig. 7

Table 4
Sr and Nd isotope ratios of bulk detritus at PZ1. Results in bold font are from Haliva-Cohen et al. (2012). Ages after Torfstein et al., 2013a.

Sample name	Height (cm)	Age (ka)	$^{87}Sr/^{86}Sr$	$^{143}Nd/^{144}Nd$	εNd
PZ1 3558	3558	18.5	0.711353	0.512250	−7.6
PZ1 3443	3443	20.2	**0.711078**	**0.512259**	−7.4
PZ1 3253	3253	22.8	**0.711542**	**0.512282**	−6.9
PZ1 3059	3059	25.5	**0.711454**	0.512267	−7.2
PZ1 2894	2894	27.8	**0.710988**	**0.512272**	−7.1
PZ1 2768	2768	29.6	**0.710704**	0.512243	−7.7
PZ1 2670	2670	30.9	**0.709620**		
PZ1 2666	2666	31.0	**0.711134**		
PZ1 2489	2489	33.5	**0.710875**	0.512250	−7.6
PZ1 2290	2290	36.2	**0.709895**		
PZ1 2274	2274	36.5	**0.708350**		
PZ1 2230	2230	37.1	**0.711046**	0.512345	−5.7
PZ1 2172	2172	37.9	**0.710579**	**0.512282**	−6.9
PZ1 2025	2025	39.9	**0.710664**	0.512323	−6.1
PZ1 1838	1838	42.5	**0.711470**	**0.512280**	−7.0
PZ1 1715	1715	49.3	**0.711945**	0.512270	−7.2
PZ1 1680	1680	49.5	**0.711251**	**0.512274**	−7.1
PZ1 1535	1535	50.4	**0.711580**	**0.512296**	−6.7
PZ1 1464	1464	50.8	**0.710238**	0.512220	−8.2
PZ1 1327	1327	51.6	**0.711638**	0.512285	−6.9
PZ1 1320	1320	51.6	**0.711059**	**0.512299**	−6.6
PZ1 827	827	56.0	**0.711282**		
PZ1 497	497	58.3	**0.710631**	0.512325	−6.1
PZ1 455	455	58.7	**0.710820**	0.512311	−6.4
PZ1 414	414	59.5	**0.710756**	0.512372	−5.2
PZ1 218	218	64.1		0.512234	−7.9
PZ1 210	210	64.3	**0.710429**		
PZ1 110	110	66.8	**0.710735**	0.512252	−7.5
PZ1 40	40	68.5	**0.711270**	0.512250	−7.6
PZ1 20	20	69.0	**0.711334**	**0.512211**	−8.3
PZ1 0	0	69.5	**0.711479**	**0.512263**	−7.3

Table 5
Sr and Nd isotope ratios of bulk detritus at the DSDDP core. Ages from Torfstein et al. (2015).

Sample name	Depth (mblf)	Age (ka)	$^{87}Sr/^{86}Sr$	$^{143}Nd/^{144}Nd$	εNd
AT 105J	2.74	0.4		0.512346	−5.7
AT-47a	16.94	2.7	0.709907	0.512290	−6.8
AT-11	44.13	7	0.708540	0.512371	−5.2
AT-13	58.2	9.1	0.708627	0.512363	−5.4
AT-36	113.72	25.9	0.709739	0.512303	−6.5
AT-37	113.78	26	0.708935	0.512298	−6.6
AT-41	138.62	42.5	0.709165	0.512292	−6.7
AT-58c	174.32	68.1	0.709420	0.512302	−6.6
AT102a	180.25	72.3		0.512332	−6.0
AT-64	201.55	87.1	0.708733	0.512341	−5.8
AT-70a	220.03	99.9	0.708756	0.512369	−5.3
AT-74a	222.91	101.9	0.709190	0.512331	−6.0
AT-72a	226.52	104.4	0.708781	0.512341	−5.8
AT-76d	241.07	117.4	0.708993	0.512305	−6.5
AT-79f	283.1	122.6	0.709384	0.512307	−6.5
AT-80	283.25	122.6	0.709846	0.512306	−6.5
AT-116a	307.42	129.1	0.709613	0.512308	−6.4
AT-89b	324.95	134.1	0.709189	0.512303	−6.5
AT-97d	394.55	190.9	0.709151	0.512347	−5.7
AT-97a	395	191	0.708592	0.512352	−5.6
AT-100b	445.8	215.2	0.709481	0.512333	−6.0

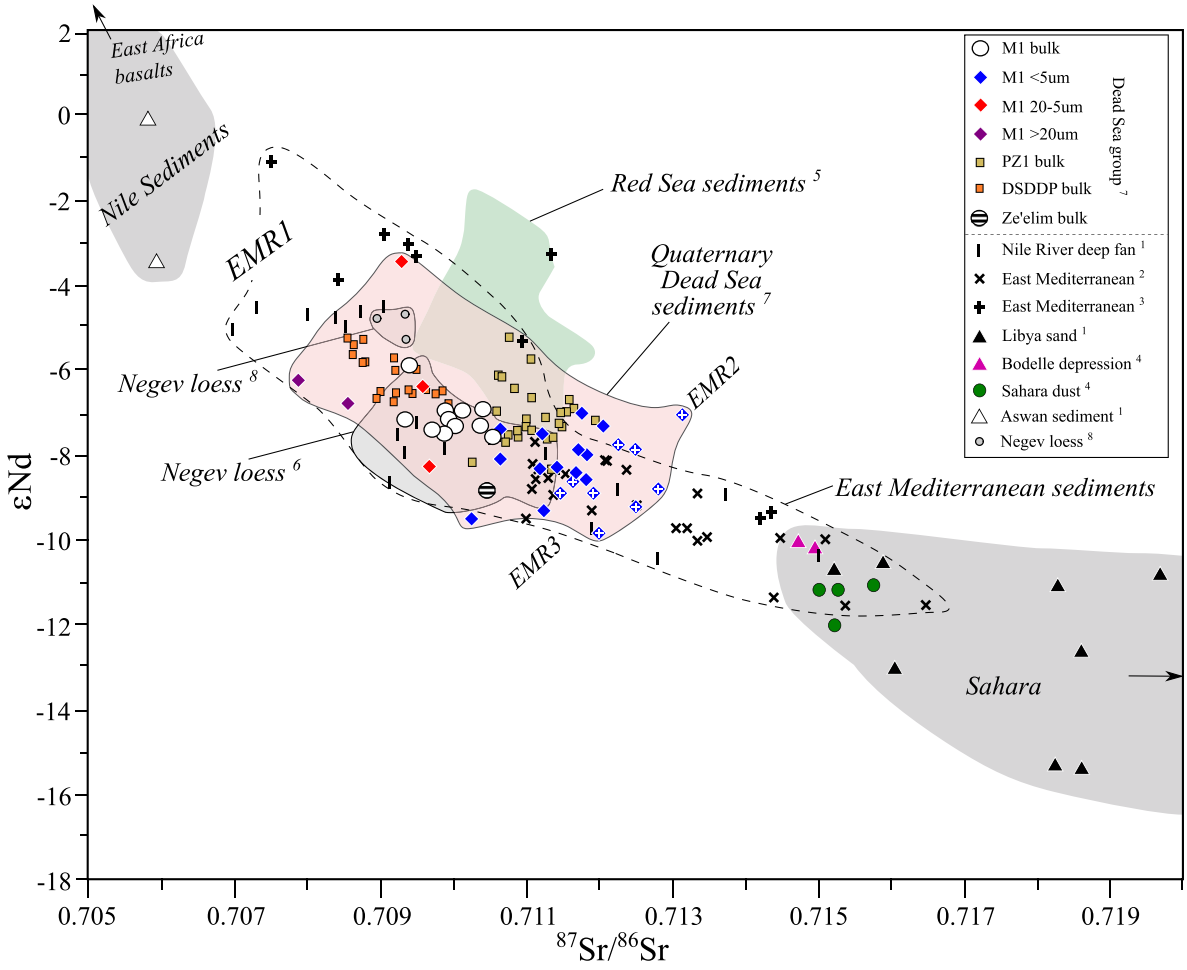

Fig. 6. $^{87}Sr/^{86}Sr$ vs εNd. Sources: [1] Revel et al. (2010), [2] Freydier et al. (2001), [3] Weldeab et al. (2002), [4] Abouchami et al. (2013), [5] Palchan et al. (2013) (core KL23), [6] <20 μm loess fraction, Ben Israel et al. (2015), [7] this work and partial PZ1 data from Haliva-Cohen et al. (2012), [8] Haliva-Cohen et al. (2012). All the samples in this diagram fall along a mixing array ranging between the composition of fine sediments and dust from the Sahara Desert and an end member associated with an intermediate composition between Nile River sediments and the composition of local loess deposits. This end member is referred to as end member 1 (EMR1; see text for details). Note that blue diamonds (<5 μm fraction at Masada) with white crosses represent the "Sahara dust array" as defined in Fig. 7. All the latter are skewed toward the lower right range of the Dead Sea sediments, indicating the dominance of the Sahara Dust end member in these samples. In itself, the "Sahara dust array" can be resolved as a mixing array (though not as prominent as in Fig. 7) between two end members – EMR2 and EMR3 – who form a positive perpendicular trend relative to the rest of the samples presented here. (For interpretation of the references to color in this figure legend, the reader is referred to the Web version of this article.)

4.2. Temporal trends in dust mobilization to the Dead Sea

Abrupt lake level drops associated with massive gypsum deposition in Lake Lisan ca. 60–58, 49–47.5 and 17.1–15.5 ka (Fig. 2b) reflect the regional response to the global climate perturbations associated with Heinrich (H) Stadials 6, 5 and 1, respectively (Hemming, 2004), which triggered short-term (millennial scale) arid-spells in the Levant, during the otherwise relatively wet last glacial cycle (Bartov et al., 2003; Torfstein et al., 2013b). In the M1 section the <5 μm fractions from those intervals are associated with the Sahara dust array (section 4.1, Fig. 7b). All of these intervals are characterized by shifts towards higher Sr and lower Nd isotope ratios in the <5 μm fraction (Figs. 3 and 6). In contrast, the Pb isotope ratios show a large range and include both the highest and lowest values. These tracers also show temporal variability, most clearly observed for Pb isotopes during H6, when the Pb isotope ratios are low compared to H1 and H5 (Fig. 7). For $^{87}Sr/^{86}Sr$ ratios, the H1 and H5 intervals show slightly higher values than H6 (Figs. 3b and 7). A temporal trend toward higher Sr isotope ratios is also seen in the bulk samples at M1 over the last glacial – Holocene cycle (dashed black arrow in Fig. 3b).

Thus, the combined Sr-Nd isotope data indicate a stronger contribution of the Saharan dust to the DSB during Heinrich events. The Pb isotope ratios show that during H6 the source was different from H5 and H1, whereby the H6 source was characterized by low $^{206}Pb/^{204}Pb$ ratios and the H5 and H1 sources had higher $^{206}Pb/^{204}Pb$ ratios (Fig. 5). These relationships in Saharan Pb isotope ratios have been observed in the central and western Sahara versus the Bodélé depression, respectively (Abouchami et al., 2013; Kumar et al., 2014), although neither region has compositions corresponding with the Saharan dust array in Fig. 7 and therefore neither can be considered direct sources of the dust in the Levant.

Outside of the Heinrich intervals, during MIS3 and early MIS2, the Sr-Nd-Pb isotope compositions in the <5 μm fraction show values closer to the loess end member composition (EMR1). This indicates a diminished contribution of Sahara dusts and increased mobilization of fine detritus from the local surface cover (e.g., loess type soils).

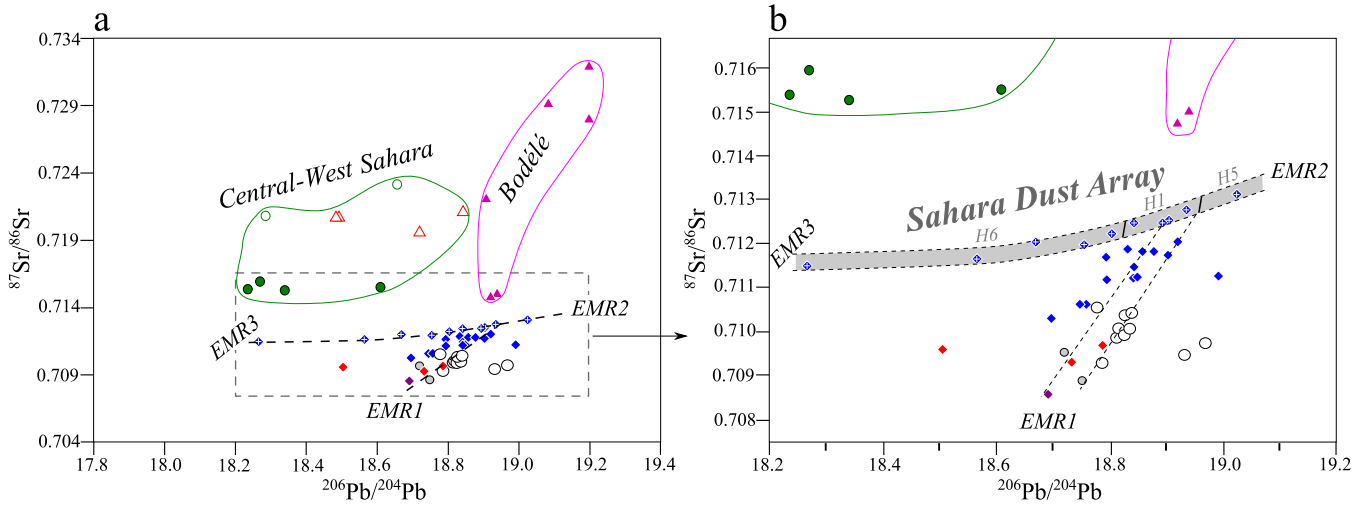

Fig. 7. $^{87}Sr/^{86}Sr$ vs $^{206}Pb/^{204}Pb$. Three compositional end members can be identified for the Dead Sea basin lacustrine deposits: the first, EMR1, is associated with relatively low and intermediate, $^{87}Sr/^{86}Sr$ and $^{206}Pb/^{204}Pb$ values, respectively. EMR1 appears to be associated with regional loess values and the coarser grain sizes within the Lisan Formation. Two other end members, EMR2 and EMR3, are characterized by minor differences in their $^{87}Sr/^{86}Sr$ composition (0.7115 and 0.7131, respectively), but a relatively larger difference in their $^{206}Pb/^{204}Pb$ composition (18.26 and 19.02, respectively). These are defined by a mixing array displayed by the fine fraction (<5 μm) and marked in panel (b) by a grey shadow. Because these samples fall close to the Sahara end member in the Sr-Nd isotope space (Fig. 6), we define the array between EMR2 and EMR3 as the "Sahara dust array". Moreover, all samples within this array are associated with Heinrich stadials, whereby EMR2 appears to be more dominant during H5 and H1 relative to H6, which is more strongly controlled by EMR3. Legend follows Fig. 6 except for samples associated with potential source regions in the Sahara, namely, Central-West Sahara dust and soils, and the Bodélé Depression (data compiled from: Abouchami et al., 2013; Kumar et al., 2014). The loess Sr and Pb values (samples LN-1 and LN-2) are from Haliva-Cohen et al. (2012) and Torfstein (2008), respectively.

4.3. Grain size effects

The temporal trends of the Sr and Nd isotope ratios of the 20-5 μm and >20 μm fractions mirror those of the fine fraction (<5 μm, Fig. 3), displaying lower $^{87}Sr/^{86}Sr$ and higher εNd values with time (although only observed for a few samples). These patterns can be considered in the context of the bulk detritus composition in the three main study sites (Fig. 2), i.e., the PZ1 and M1 subaerial sections, and the ICDP-DSDDP deep basin core. While the εNd roughly overlap in all sites (Fig. 3c), the $^{87}Sr/^{86}Sr$ ratios display distinct differences (Fig. 3d), with higher values at the shallower sites (Fig. 8). At PZ1, this comparison excludes three samples of massive marl beds associated with an MIS3 low stand (Haliva-Cohen et al., 2012), which display significantly lower $^{87}Sr/^{86}Sr$ values (marked as circles in Fig. 8). This "tail" in PZ1 is consistent with the characteristic $^{87}Sr/^{86}Sr$ fingerprints in the different grain sizes at M1 (Fig. 3), where coarse (>5 μm) particles have lower values than fine particles (<5 μm). The observation that the different grain size populations have distinct isotopic compositions means that the main factor controlling the bulk composition is the grain size distribution. This suggests, based on the Sr isotopic composition (Fig. 8), that the average grain size mode in the DSB lacustrine system increases with depth of the deposition site. The current lack of systematic grain size analyses however, precludes further discussion of this observation.

4.4. Sahara dust during heinrich stadials and implications for global climate

The results of this study indicate that distally delivered atmospheric (suspended) dust in the Lisan Formation (associated with the <5 μm fraction) became dominant during H stadials, when lake levels were low compared to the glacial norm (Bartov et al., 2003; Torfstein et al., 2013b). In general, dust loads are understood to be globally high during glacial cycles (e.g., Kohfeld and Harrison, 2001), with more limited evidence supporting high dust loads associated with the Sahara Desert during the Last Glacial Maximum (LGM) and the last deglaciation (Cole et al., 2009; Roberts et al., 2011; McGee et al., 2013).

Considering that the LGM was extremely wet in the Levant, it is reasonable that dust fluxes from the Sahara were suppressed by wet deposition, while hyper-arid spells during H-stadial intervals (as reflected, for example, by sharp lake level drops) were accompanied by enhanced supply of fine Sahara dusts to the vicinity of the Dead Sea. This was probably further intensified due to increased wind speed and gustiness of west winds that had been suggested to prevail in the Sahara – East Mediterranean region during H-stadials (Palchan et al., 2018; Rohling, 2013). Thus, the influence of Levant hydroclimate imposed a regional history of dust delivery that is somewhat different from general global trends, thus suggesting that local climate conditions often have primary impacts on reconstructions of dust provenance in continental settings.

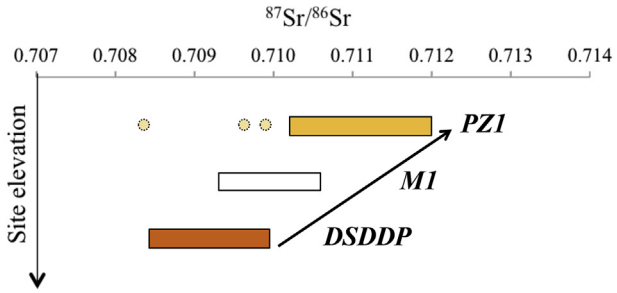

Fig. 8. The range of bulk detritus $^{87}Sr/^{86}Sr$ ratios in sites from different elevations along the DSB. Note that the shallower the site, the more radiogenic the composition of its sediments. Three samples from PZ1, marked by circles, are associated with massive marl beds (the laminar-detritus facies, rather than fine detritus from the alternating aragonite–detritus facies; Haliva-Cohen et al., 2012) display significantly lower values and are excluded from this comparison.

5. Conclusions

The Sr-Nd-Pb isotope compositions of grain size fractions (>20, 20–5, <5 μm) and bulk detritus (siliciclastic) samples of lacustrine deposits from the Dead Sea Basin, were studied at Masada (M1 section), Perazim Valley (PZ1 section), and the ICDP-DSDDP core extracted from the deep center of the modern lake. The finest grain size fraction (<5 μm) is associated with atmospheric dust that predominantly originated from the Sahara Desert, with a strong control of two end member compositions (EMR2, EMR3), which form a range of Sr-Pb isotope ratios defined here as the "Sahara dust array". Although the geographic source of these two end members remains unknown, it is likely independent of the compositions of modern dust and soils in the Bodélé Depression and additional sites in central-west Sahara.

The "Sahara dust array" is dominated by samples deposited in Lake Lisan during Heinrich (H) stadials 6, 5 and 1. These time intervals are associated with extreme dry-spells in the Levant. Moreover, the "Sahara dust array" shows that the source of atmospheric dust to the Dead Sea Basin changed over time, with relatively low $^{87}Sr/^{86}Sr$ and $^{206}Pb/^{204}Pb$ ratios (EMR3) characterizing H6, and higher $^{87}Sr/^{86}Sr$ and $^{206}Pb/^{204}Pb$ ratios (EMR2) characterizing H5 and H1. By contrast, the coarser grain size fractions display a closer resemblance to regional loess compositions (EMR1).

Although dust fluxes are assumed to have been globally high during the LGM, an extremely wet glacial cycle in the Levant suppressed the transport of dust to this region. During Heinrich stadials however, the delivery of fine Sahara dust intensified due to a combination between strong westerly winds and hyperarid conditions in the Levant.

Acknowledgments

We wish to thank Louise Bolge and Jason Jweda for assistance in the lab. We further thank two anonymous reviewers for their thoughtful comments and Xiaoping Yang for editorial handling. Funding was provided by the USA-Israel Bi-National Science Foundation project #2010375 (to MS and SLG), the Israel Science Foundation grant 927/15 (to AT), Comer Science & Education Foundation grant #CP69 (to AT), and the Dead Sea Drill Center of Excellence of the Israel Science Foundation (grants 1736/11 and 1436/14 to MS). This is LDEO contribution #8186.

References

Aarons, S.M., Aciego, S.M., Gleason, J.D., 2013. Variable Hf-Sr-Nd radiogenic isotopic compositions in a Saharan dust storm over the Atlantic: implications for dust flux to oceans, ice sheets and the terrestrial biosphere. Chem. Geol. 349–350, 18–26. Available at. https://doi.org/10.1016/j.chemgeo.2013.04.010.

Aarons, S.M., Aciego, S.M., Gabrielli, P., Delmonte, B., Koornneef, J.M., Wegner, A., Blakowski, M.A., 2016. The impact of glacier retreat from the Ross Sea on local climate: characterization of mineral dust in the Taylor Dome ice core, East Antarctica. Earth Planet Sci. Lett. 444, 34–44. Available at. https://doi.org/10.1016/j.epsl.2016.03.035.

Abouchami, W., Galer, S., Koschinsky, A., 1999. Pb and Nd isotopes in NE Atlantic Fe – Mn crusts: proxies for trace metal paleosources and paleocean circulation. Geochem. Cosmochim. Acta 63, 1489–1505. Available at. http://www.sciencedirect.com/science/article/pii/S001670379900068X.

Abouchami, W., Näthe, K., Kumar, A., Galer, S.J.G., Jochum, K.P., Williams, E., Horbe, A.M.C., Rosa, J.W.C., Balsam, W., Adams, D., Mezger, K., Andreae, M.O., 2013. Geochemical and isotopic characterization of the bodélé depression dust source and implications for transatlantic dust transport to the Amazon basin. Earth Planet Sci. Lett. 380, 112–123. Available at. https://doi.org/10.1016/j.epsl.2013.08.028.

Allègre, C., Dupré, B., Négrel, P., Gaillardet, J., 1996. Sr-Nd-Pb isotope systematics in Amazon and Congo River systems: constraints about erosion processes. Chem. Geol. 131, 93–112. Available at. http://www.sciencedirect.com/science/article/pii/0009254196000289.

Baker, J., Peate, D., Waight, T., Meyzen, C., 2004. Pb isotopic analysis of standards and samples using a 207 Pb – 204 Pb double spike and thallium to correct for mass bias with a double-focusing MC-ICP-MS. Chem. Geol. 211, 275–303.

Bar-Matthews, M., Ayalon, A., Gilmour, M., Matthews, A., Hawksworth, C.J., 2003. Sea–land oxygen isotopic relationships from planktonic foraminifera and speleothems in the Eastern Mediterranean region and their implication for paleorainfall during. Geochem. Cosmochim. Acta 67, 3181–3199. Available at. http://www.sciencedirect.com/science/article/pii/S0016703702010311.

Bartov, Y., Goldstein, S.L., Stein, M., Enzel, Y., 2003. Catastrophic arid episodes in the eastern mediterranean linked with the north atlantic Heinrich events. Geology 31, 439–442.

Bayon, G., Burton, K.W., Soulet, G., Vigier, N., Dennielou, B., Etoubleau, J., Ponzevera, E., German, C.R., Nesbitt, R.W., 2009. Hf and Nd isotopes in marine sediments: constraints on global silicate weathering. Earth Planet Sci. Lett. 277, 318–326. Available at. https://doi.org/10.1016/j.epsl.2008.10.028.

Ben Israel, M., Enzel, Y., Amit, R., Erel, Y., 2015. Provenance of the various grain-size fractions in the Negev loess and potential changes in major dust sources to the Eastern Mediterranean. Quat. Res. (United States) 83, 105–115. Available at. https://doi.org/10.1016/j.yqres.2014.08.001.

Blakowski, M.A., Aciego, S.M., Delmonte, B., Baroni, C., Cristina, M., Sims, K.W.W., 2016. A Sr-Nd-Hf isotope characterization of dust source areas in Victoria Land and the McMurdo Sound sector of Antarctica. Quat. Sci. Rev. 141, 26–37. Available at. https://doi.org/10.1016/j.quascirev.2016.03.023.

Bookman (Ken-Tor), R., Enzel, Y., Agnon, A., Stein, M., 2004. Late Holocene lake levels of the Dead Sea. Geol. Soc. Am. Bull. 116, 555–571. Available at. http://gsabulletin.gsapubs.org/cgi/doi/10.1130/B25286.1.

Bouvier, A., Vervoort, J.D., Patchett, P.J., 2008. The Lu-Hf and Sm-Nd isotopic composition of CHUR: constraints from unequilibrated chondrites and implications for the bulk composition of terrestrial planets. Earth Planet Sci. Lett. 273, 48–57.

Box, M.R., Krom, M.D., Cliff, R. a., Bar-Matthews, M., Almogi-Labin, a., Ayalon, a., Paterne, M., 2011. Response of the Nile and its catchment to millennial-scale climatic change since the LGM from Sr isotopes and major elements of East Mediterranean sediments. Quat. Sci. Rev. 30, 431–442. Available at. http://linkinghub.elsevier.com/retrieve/pii/S027737911000435X.

Cole, J.M., Goldstein, S.L., deMenocal, P.B., Hemming, S.R., Grousset, F.E., 2009. Contrasting compositions of saharan dust in the eastern atlantic ocean during the last deglaciation and african humid period. Earth Planet Sci. Lett. 278, 257–266. Available at. http://linkinghub.elsevier.com/retrieve/pii/S0012821X08007590.

Crouvi, O., Amit, R., Enzel, Y., Porat, N., Sandler, A., 2008. Sand dunes as a major proximal dust source for late Pleistocene loess in the Negev Desert. Israel. Quat. Res. 70, 275–282. Available at. http://linkinghub.elsevier.com/retrieve/pii/S0033589408000732. (Accessed 15 September 2013).

Dayan, U., 1986. Climatology of back trajectories from Israel based on synoptic analysis. J. Clim. Appl. Meteorol. 25, 591–595.

Elburg, M., Vroon, P., van der Wagt, B., Tchalikian, A., 2005. Sr and Pb isotopic composition of five USGS glasses (BHVO-2G, BIR-1G, BCR-2G, TB-1G, NKT-1G). Chem. Geol. 223, 196–207.

Enzel, Y., Bookman (Ken Tor), R., Sharon, D., Gvirtzman, H., Dayan, U., Ziv, B., Stein, M., 2003. Late Holocene climates of the Near East deduced from Dead Sea level variations and modern regional winter rainfall. Quat. Res. (Duluth) 60, 263–273. Available at. http://linkinghub.elsevier.com/retrieve/pii/S0033589403001261.

Enzel, Y., Amit, R., Dayan, U., Crouvi, O., Kahana, R., Ziv, B., Sharon, D., 2008. The climatic and physiographic controls of the eastern Mediterranean over the late Pleistocene climates in the southern Levant and its neighboring deserts. Global Planet. Change 60, 165–192. Available at. http://linkinghub.elsevier.com/retrieve/pii/S0921818107000240.

Freydier, R., Michard, A., De, Lange G., Thomson, J., 2001. Nd isotopic compositions of Eastern Mediterranean sediments: tracers of the Nile influence during sapropel S1 formation? Mar. Geol. 177, 45–62. Available at. http://www.sciencedirect.com/science/article/pii/S0025322701001232.

Frumkin, A., Stein, M., 2004. The Sahara–East Mediterranean dust and climate connection revealed by strontium and uranium isotopes in a Jerusalem speleothem. Earth Planet Sci. Lett. 217, 451–464. Available at. http://linkinghub.elsevier.com/retrieve/pii/S0012821X03005892.

Gaiero, D.M., 2007. Dust provenance in Antarctic ice during glacial periods: from where in southern South America? Geophys. Res. Lett. 34, L17707. Available at. http://doi.wiley.com/10.1029/2007GL030520.

Gaiero, D.M., Brunet, F., Probst, J.-L., Depetris, P.J., 2007. A uniform isotopic and chemical signature of dust exported from Patagonia: rock sources and occurrence in southern environments. Chem. Geol. 238, 107–120. Available at. http://linkinghub.elsevier.com/retrieve/pii/S000925410600502X.

Ganor, E., Foner, H.A., 2001. Mineral dust concentrations, deposition fluxes and deposition velocities in dust episodes over Israel. J. Geophys. Res. 106, 18431. Available at. http://onlinelibrary.wiley.com/doi/10.1029/2000JD900535/full.

Ganor, E., Mamane, Y., 1982. Transport of saharan dust across the eastern mediterranean. Atmos. Environ. 16, 581–587. Available at. http://linkinghub.elsevier.com/retrieve/pii/0004698182901676.

Gasse, F., 2000. Hydrological changes in the african tropics since the last glacial Maximum. Quat. Sci. Rev. 19, 189–211. Available at. http://linkinghub.elsevier.com/retrieve/pii/S027737919900061X.

Gili, S., Gaiero, D.M., Goldstein, S.L., Chemale, F., Koester, E., Jweda, J., Vallelonga, P., Kaplan, M.R., 2016. Provenance of dust to Antarctica: a lead isotopic perspective. Geophys. Res. Lett. 43, 2291–2298.

Gili, S., Gaiero, D.M., Goldstein, S.L., Chemale, F., Jweda, J., Kaplan, M.R., Becchio, R.A., Koester, E., 2017. Glacial/interglacial changes of Southern Hemisphere wind

circulation from the geochemistry of South American dust. Earth Planet Sci. Lett. 469, 98–109. Available at. https://doi.org/10.1016/j.epsl.2017.04.007.
Goldstein, S., Jacobsen, S., 1988. Nd and Sr isotopic systematics of river water suspended material: implications for crustal evolution. Earth Planet Sci. Lett. 87, 249–265. Available at. http://www.sciencedirect.com/science/article/pii/0012821X88900131.
Goldstein, S.L., O'Nions, R., Hamilton, P., 1984. A Sm-Nd isotopic study of atmospheric dusts and particulates from major river systems. Earth Planet Sci. Lett. 70, 221–236.
Grousset, F.E., Biscaye, P.E., 2005. Tracing dust sources and transport patterns using Sr, Nd and Pb isotopes. Chem. Geol. 222, 149–167. Available at. http://linkinghub.elsevier.com/retrieve/pii/S0009254105002202.
Grousset, F.E., Biscaye, P.E., Revel, M., Petit, J.-R., Pye, K., Joussaume, S., Jouzel, J., 1992. Antarctic (Dome C) ice-core dust at 18 k.y. B.P.: isotopic constraints on origins. Earth Planet Sci. Lett. 111, 175–182. Available at. http://linkinghub.elsevier.com/retrieve/pii/0012821X9290177W.
Haase-Schramm, A., Goldstein, S.L., Stein, M., 2004. U-Th dating of Lake Lisan (late Pleistocene dead sea) aragonite and implications for glacial east Mediterranean climate change. Geochem. Cosmochim. Acta 68, 985–1005. Available at. http://linkinghub.elsevier.com/retrieve/pii/S0016703703005647.
Haliva-Cohen, A., Stein, M., Goldstein, S.L., Sandler, A., Starinsky, A., 2012. Sources and transport routes of fine detritus material to the Late Quaternary Dead Sea basin. Quat. Sci. Rev. 50, 55–70. Available at. http://www.sciencedirect.com/science/article/pii/S0277379112002454.
Hemming, S., 2004. Heinrich events: massive late Pleistocene detritus layers of the North Atlantic and their global imprint. Rev. Geophys. 42, 2003RG000128. Available at. http://onlinelibrary.wiley.com/doi/10.1029/2003RG000128/full.
Hyeong, K., Kim, J., Pettke, T., Yoo, C.M., Hur, S., 2011. Lead, Nd and Sr isotope records of pelagic dust: source indication versus the effects of dust extraction procedures and authigenic mineral growth. Chem. Geol. 286, 240–251. Available at. http://linkinghub.elsevier.com/retrieve/pii/S0009254111002099.
Israelevich, P.L., Ganor, E., Levin, Z., Joseph, J.H., 2003. Annual variations of physical properties of desert dust over Israel. J. Geophys. Res. 108, 1–9.
Jickells, T.D., An, Z.S., Andersen, K.K., Baker, A.R., Bergametti, G., Brooks, N., Cao, J.J., Boyd, P.W., Duce, R.A., Hunter, K.A., Kawahata, H., Kubilay, N., LaRoche, J., Liss, P.S., Mahowald, N., Prospero, J.M., Ridgwell, A.J., Tegen, I., Torres, R., 2005. Global iron connections between desert dust, ocean biogeochemistry, and climate. Science 308, 67–71. Available at. http://www.ncbi.nlm.nih.gov/pubmed/15802595.
Jweda, J., Bolge, L., Class, C., Goldstein, S.L., 2016. High precision Sr-Nd-Hf-Pb isotopic compositions of USGS reference material BCR-2. Geostand. Geoanal. Res. 40, 101–115.
Kalderon-Asael, B., Erel, Y., Sandler, A., Dayan, U., 2009. Mineralogical and chemical characterization of suspended atmospheric particles over the east Mediterranean based on synoptic-scale circulation patterns. Atmos. Environ. 43, 3963–3970. Available at. http://linkinghub.elsevier.com/retrieve/pii/S1352231009003057.
Katz, A., Kolodny, Y., Nissenbaum, A., 1977. The geochemical evolution of the pleistocene Lake Lisan-Dead Sea system. Geochem. Cosmochim. Acta 41, 1609–1626. Available at. http://www.sciencedirect.com/science/article/pii/0016703777901727.
Kohfeld, K.E., Harrison, S.P., 2001. DIRTMAP: the geological record of dust. Earth Sci. Rev. 54, 81–114.
Kumar, a, Abouchami, W., Galer, S.J.G., Garrison, V.H., Williams, E., Andreae, M.O., 2014. A radiogenic isotope tracer study of transatlantic dust transport from Africa to the Caribbean. Atmos. Environ. 82, 130–143. Available at. https://doi.org/10.1016/j.atmosenv.2013.10.021.
Kushnir, Y., Stein, M., 2010. North Atlantic influence on 19th–20th century rainfall in the Dead Sea watershed, teleconnections with the Sahel, and implication for Holocene climate fluctuations. Quat. Sci. Rev. 29, 3843–3860. Available at. http://linkinghub.elsevier.com/retrieve/pii/S0277379110003264.
Lisker, S., Vaks, A., Bar-Matthews, M., Porat, R., Frumkin, A., 2009. Stromatolites in caves of the Dead Sea Fault Escarpment: implications to latest Pleistocene lake levels and tectonic subsidence. Quat. Sci. Rev. 28, 80–92. Available at. http://linkinghub.elsevier.com/retrieve/pii/S0277379108002849.
Machlus, M., Enzel, Y., Goldstein, S.L., Marco, S., Stein, M., 2000. Reconstructing low levels of Lake Lisan by correlating fan-delta and lacustrine deposits. Quat. Int. 73–74, 137–144. Available at. http://linkinghub.elsevier.com/retrieve/pii/S1040618200000707.
Mahowald, N.M., Engelstaedter, S., Luo, C., Sealy, A., Artaxo, P., Benitez-Nelson, C., Bonnet, S., Chen, Y., Chuang, P.Y., Cohen, D.D., Dulac, F., Herut, B., Johansen, A.M., Kubilay, N., Losno, R., Maenhaut, W., Paytan, A., Prospero, J.M., Shank, L.M., Siefert, R.L., 2009. Atmospheric iron deposition: global distribution, variability, and human perturbations. Ann. Rev. Mar. Sci. 1, 245–278. Available at. http://www.ncbi.nlm.nih.gov/pubmed/21141037.
McGee, D., deMenocal, P.B., Winckler, G., Stuut, J.B.W., Bradtmiller, L.I., 2013. The magnitude, timing and abruptness of changes in North African dust deposition over the last 20,000yr. Earth Planet Sci. Lett. 371–372, 163–176. Available at. http://linkinghub.elsevier.com/retrieve/pii/S0012821X13001817.
Meyer, I., Davies, G.R., Stuut, J.-B.W., 2011. Grain size control on Sr-Nd isotope provenance studies and impact on paleoclimate reconstructions: an example from deep-sea sediments offshore NW Africa. G-cubed 12 n/a-n/a. Available at. http://doi.wiley.com/10.1029/2010GC003355.
Migowski, C., Stein, M., Prasad, S., Negendank, J.F.W., Agnon, A., 2006. Holocene climate variability and cultural evolution in the Near East from the Dead Sea sedimentary record. Quat. Res. (Duluth) 66, 421–431. Available at. http://linkinghub.elsevier.com/retrieve/pii/S0033589406000925.
Neugebauer, I., Brauer, A., Schwab, M.J., Waldmann, N., Enzel, Y., Kitagawa, H., Torfstein, A., Frank, U., Dulski, P., Agnon, A., Ariztegui, D., Ben-Avraham, Z., Goldstein, S.L., Stein, M., 2014. Lithology of the long sediment record recovered by the ICDP Dead Sea deep drilling project (DSDDP). Quat. Sci. Rev. 102, 149–165. Available at. http://www.sciencedirect.com/science/article/pii/S0277379114003333.
Palchan, D., Stein, M., Almogi-Labin, a., Erel, Y., Goldstein, S.L., 2013. Dust transport and synoptic conditions over the Sahara–Arabia deserts during the MIS6/5 and 2/1 transitions from grain-size, chemical and isotopic properties of Red Sea cores. Earth Planet Sci. Lett. 382, 125–139. Available at. http://linkinghub.elsevier.com/retrieve/pii/S0012821X13005153.
Palchan, D., Stein, M., Goldstein, S.L., Almogi-Labin, A., Tirosh, O., Erel, Y., 2018. Synoptic conditions of fine-particle transport to the last interglacial Red Sea-Dead Sea from Nd-Sr compositions of sediment cores. Quat. Sci. Rev. 179, 123–136. Available at. http://linkinghub.elsevier.com/retrieve/pii/S0277379116307429.
Pichat, S., Abouchami, W., Galer, S.J.G., 2014. Lead isotopes in the eastern equatorial pacific record quaternary migration of the south westerlies. Earth Planet Sci. Lett. 388, 293–305. Available at. https://doi.org/10.1016/j.epsl.2013.11.035.
Pourmand, A., Prospero, J.M., Sharifi, A., 2014. Geochemical fingerprinting of trans-Atlantic African dust based on radiogenic Sr-Nd-Hf isotopes and rare earth element anomalies. Geology 42, 675–678.
Prasad, S., Vos, H., Negendank, J.F.W., Waldmann, N., Goldstein, S.L., Stein, M., 2004. Evidence from Lake Lisan of solar influence on decadal- to centennial-scale climate variability during marine oxygen isotope stage 2. Geology 32, 581. Available at. http://geology.gsapubs.org/cgi/doi/10.1130/G20553.1.
Prospero, J.M., Nees, R.T., 1977. Dust concentration in the atmosphere of the equatorial north atlantic: possible relationship to the sahelian drought. Science 196, 1196–1198.
Prospero, J.M., Ginoux, P., Torres, O., Nicholson, S., Gill, T.E., 2002. Environmental characterization of global sources of atmospheric soil dust identified with the NIMBUS 7 Total Ozone Mapping Spectrometer (TOMS) absorbing aerosol product. Rev. Geophys. 40, 1002. Available at. http://doi.wiley.com/10.1029/2000RG000095.
Pye, K., Zhou, L.-P., 1989. Late Pleistocene and Holocene aeolian dust deposition in north China and the northwest Pacific Ocean. Palaeogeogr. Palaeoclimatol. Palaeoecol. 73, 11–23.
Rabi, R., 2004. Geochemical Characterization of Suspended Desert Dust in Israel. MSc thesis. Hebrew University of Jerusalem.
Revel, M., Ducassou, E., Grousset, F.E., Bernasconi, S.M., Migeon, S., Revillon, S., Mascle, J., Murat, a., Zaragosi, S., Bosch, D., 2010. 100,000 Years of African monsoon variability recorded in sediments of the Nile margin. Quat. Sci. Rev. 29, 1342–1362. Available at. http://linkinghub.elsevier.com/retrieve/pii/S0277379110000387.
Roberts, A.P., Rohling, E.J., Grant, K.M., Larrasoaña, J.C., Liu, Q., 2011. Atmospheric dust variability from Arabia and China over the last 500,000 years. Quat. Sci. Rev. 30, 3537–3541. Available at. https://doi.org/10.1016/j.quascirev.2011.09.007.
Rohling, E., 2013. Quantitative assessment of glacial fluctuations in the level of Lake Lisan, Dead Sea rift. Quat. Sci. Rev. 70, 63–72. Available at. http://www.sciencedirect.com/science/article/pii/S0277379113001182. (Accessed 13 April 2014).
Schramm, A., Stein, M., Goldstein, S., 2000. Calibration of the 14 C time scale to >40 ka by 234 U– 230 Th dating of Lake Lisan sediments (last glacial Dead Sea). Earth Planet Sci. Lett. 175, 27–40. Available at. http://www.sciencedirect.com/science/article/pii/S0012821X99002794.
Schutz, L., Jaenicke, R., Pietrek, H., 1981. Saharan dust transport over the North Atlantic Ocean - model calculations and measurements. Geol. Soc. Am. Spec. Pap. 186, 87–100.
Skonieczny, C., Bory, a., Bout-Roumazeilles, V., Abouchami, W., Galer, S.J.G., Crosta, X., Diallo, a., Ndiaye, T., 2013. A three-year time series of mineral dust deposits on the West African margin: sedimentological and geochemical signatures and implications for interpretation of marine paleo-dust records. Earth Planet Sci. Lett. 364, 145–156. Available at. http://linkinghub.elsevier.com/retrieve/pii/S0012821X1300006X.
Stein, M., 2001. The sedimentary and geochemical record of Neogene-Quaternary water bodies in the Dead Sea Basin – inferences for the regional paleoclimatic history. J. Paleolimnol. 26, 271–282. Available at. http://link.springer.com/article/10.1023/A:1017529228186.
Stein, M., 2014. The evolution of neogene-quaternary water- bodies in the Dead Sea rift valley. In: Garfunkel, Z., Ben-Avraham, Z., Kagan, E. (Eds.), Dead Sea Transform Fault System: Reviews. Modern Approaches in Solid Earth Sciences. Springer Netherlands, Dordrecht, pp. 279–316. Available at. http://link.springer.com/10.1007/978-94-017-8872-4.
Stein, M., Starinsky, A., Katz, A., Goldstein, S.L., Machlus, M., Schramm, A., 1997. Strontium isotopic, chemical, and sedimentological evidence for the evolution of Lake Lisan and the Dead Sea. Geochem. Cosmochim. Acta 61, 3875–3992.
Stein, M., Almogi-Labin, A., Goldstein, S.L., Hemleben, C., Starinsky, A., 2007. Late Quaternary changes in desert dust inputs to the Red Sea and Gulf of Aden from 87Sr/86Sr ratios in deep-sea cores. Earth Planet Sci. Lett. 261, 104–119. Available at. http://linkinghub.elsevier.com/retrieve/pii/S0012821X07003780.
Stein, M., Torfstein, A., Gavrieli, I., Yechieli, Y., 2010. Abrupt aridities and salt deposition in the post-glacial Dead Sea and their North Atlantic connection.

Quat. Sci. Rev. 29, 567–575. Available at. http://linkinghub.elsevier.com/retrieve/pii/S0277379109003606.
Tanaka, T., Togashi, S., Kamioka, H., Amakawa, H., Kagami, H., Hamamoto, T., Yuhara, M., Orihashi, Y., Yoneda, S., Shimizu, H., Kunimaru, T., 2000. JNdi-1: a neodymium isotopic reference in consistency with LaJolla neodymium. Chem. Geol. 168, 279–281.
Torfstein, A., 2008. Brine–freshwater interplay and effects on the evolution of saline lakes: the Dead Sea rift terminal lakes. Geol. Surv. Isr. Rep. GSI/20/2008.
Torfstein, A., Gavrieli, I., Stein, M., 2005. The sources and evolution of sulfur in the hypersaline Lake Lisan (paleo-Dead Sea). Earth Planet Sci. Lett. 236, 61–77. Available at. http://www.sciencedirect.com/science/article/B6V61-4GDSF43-3/2/52ea0c9a19934b01a972fead27e48e4a.
Torfstein, A., Gavrieli, I., Katz, A., Kolodny, Y., Stein, M., 2008. Gypsum as a monitor of the paleo-limnological–hydrological conditions in Lake lisan and the Dead Sea. Geochem. Cosmochim. Acta 72, 2491–2509.
Torfstein, A., Goldstein, S., Kagan, E.J., Stein, M., 2013a. Integrated multi-site U–Th chronology of the last glacial Lake Lisan. Geochem. Cosmochim. Acta 104, 210–231.
Torfstein, A., Goldstein, S.L., Stein, M., Enzel, Y., 2013b. Impacts of abrupt climate changes in the levant from last glacial Dead Sea levels. Quat. Sci. Rev. 69, 1–7.
Torfstein, A., Goldstein, S.L., Kushnir, Y., Enzel, Y., Haug, G., Stein, M., 2015. Dead Sea drawdown and monsoonal impacts in the Levant during the last interglacial. Earth Planet Sci. Lett. 412, 235–244.
Vaks, A., Bar-Matthews, M., Ayalon, A., Schilman, B., Gilmour, M., Hawkesworth, C.J., Frumkin, A., Kaufman, A., Matthews, A., 2003. Paleoclimate reconstruction based on the timing of speleothem growth and oxygen and carbon isotope composition in a cave located in the rain shadow in Israel. Quat. Res. (Duluth) 59, 182–193. Available at. http://linkinghub.elsevier.com/retrieve/pii/S0033589403000139.
Vaks, A., Bar-Matthews, M., Ayalon, A., Matthews, A., Frumkin, A., Dayan, U., Halicz, L., Almogi-Labin, A., Schilman, B., 2006. Paleoclimate and location of the border between Mediterranean climate region and the Saharo–Arabian Desert as revealed by speleothems from the northern Negev Desert, Israel. Earth Planet Sci. Lett. 249, 384–399. Available at. http://linkinghub.elsevier.com/retrieve/pii/S0012821X06005000.
Waldmann, N., Torfstein, A., Stein, M., 2010. Northward intrusions of low- and mid-latitude storms across the Saharo-Arabian belt during past interglacials. Geology 38, 567–570. Available at. http://geology.gsapubs.org/cgi/doi/10.1130/G30654.1.
Wasserburg, G., Jacousen, S., DePaolo, D., McCulloch, M., Wen, T., 1981. Precise determination of ratios, Sm and Nd isotopic abundances in standard solutions. Geochem. Cosmochim. Acta 45, 2311–2323.
Weldeab, S., Emeis, K.-C., Hemleben, C., Vennemann, T.W., Schulz, H., 2002. Sr and Nd isotope composition of Late Pleistocene sapropels and nonsapropelic sediments from the Eastern Mediterranean Sea : implications for detrital influx and climatic conditions in the source areas. Geochem. Cosmochim. Acta 66, 3585–3598.
Wolff, E.W., Chappellaz, J., Blunier, T., Rasmussen, S.O., Svensson, A., 2010. Millennial-scale variability during the last glacial: the ice core record. Quat. Sci. Rev. 29, 2828–2838.